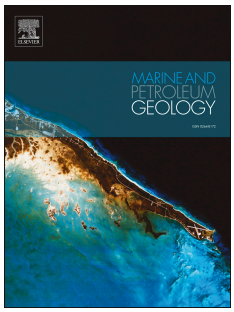

A pseudo-kinetic model to simulate phase changes in gas hydrate bearing sediments

Mehdi Teymouri, Marcelo Sánchez, J. Carlos Santamarina

PII: S0264-8172(20)30302-0

DOI: https://doi.org/10.1016/j.marpetgeo.2020.104519

Reference: JMPG 104519

To appear in: *Marine and Petroleum Geology*

Received Date: 12 October 2019

Revised Date: 3 June 2020

Accepted Date: 4 June 2020

Please cite this article as: Teymouri, M., Sánchez, M., Santamarina, J.C., A pseudo-kinetic model to simulate phase changes in gas hydrate bearing sediments, *Marine and Petroleum Geology* (2020), doi: https://doi.org/10.1016/j.marpetgeo.2020.104519.

CRediT author statement

Mehdi Teymouri: Methodology, Software, Validation, Writing - Original Draft **Marcelo Sanchez**: Conceptualization, Supervision, Funding acquisition, Writing - Original Draft; J.**Carlos Santamarina:** Supervision, Funding acquisition, Writing- Reviewing and Editing.

SUBMISSION TO: 'Marine and Petroleum Geology'

DATE:

May 31st 2020

TITLE:

A Pseudo-Kinetic Model to Simulate Phase Changes in Gas Hydrate Bearing Sediments

AUTHORS:

Mehdi Teymouri[1,2], Marcelo Sánchez[1], J. Carlos Santamarina[3]

POSITION & AFFILIATIONS:

[1] Zachry Department of Civil and Environmental Engineering, Texas A&M University, College Station, TX-USA.

[2] Hildebrand Department of Petroleum and Geosystems Engineering, the University of Texas at Austin, Austin, TX-USA.

[3] Earth Science and Engineering, King Abdullah University of Science and Technology, Thuwal, Saudi Arabia

CORRESPONDING AUTHOR:

Dr. Marcelo Sánchez
Professor
Zachry Department of Civil Engineering
Texas A&M University
College Station Texas
77843-3136, USA
Telephone: (+1) 979 862 6604
Fax: (+1) 979 862 7696
E-mail: msanchez@civil.tamu.edu

Abstract

Modeling of the phase transitions anticipated in gas hydrate bearing sediments (GHBS) is critical for a proper understanding of time-dependent changes in states and volumes (e.g. the production of methane from this type of soils). We propose a new pseudo-kinetic approach to simulate the typical phase changes anticipated in GHBS, using published experimental results involving gas hydrate dissociation that are the basis of a widely used kinetic model. The proposed pseudo-kinetic model is formulated in the pressure-temperature (*P*-*T*) plane and assumes a rate of gas hydrate dissociation (or formation) proportional to the distance between the current state and the phase boundary. The model consists of only one parameter and is simple to implement in numerical simulators. A similar concept is used to model ice formation/thawing phenomena, but based on the ice/liquid-water phase boundary. We implemented the pseudo-kinetic model in a fully coupled thermo-hydro-chemo-mechanical (THCM) finite element code and validated it against experimental results performed on the dissociation of synthetic gas hydrate. We also evaluated the pseudo-kinetic model using synthetic cases covering several scenarios associated with gas hydrate formation/dissociation and ice formation/thawing. The model successfully reproduced the gas production test from a natural GHBS core from Korea (scaled gas venting experiment over 14hours), and also the formation of gas hydrate and ice in permafrost in Alaska (over $2x10^6$ years). We show the versatility of the proposed approach by applying it to model the different phase transitions typically encounter in GHBS. The simple formulation, easy implementation in numerical simulator, and reduced number of parameters (only one per phase change) make this model an attractive option for simulating phase transformations in problems involving GHBS.

Keywords: gas hydrate; hydrate dissociation; hydrate formation; ice formation/melting; phase transitions; numerical modeling; validation.

1. Introduction

Gas hydrate bearing sediments (GHBS) represent the largest global reserve of hydrocarbons (Sloan, 1998; Soga et al., 2006; Makogon et al., 2007; Rutqvist & Moridis, 2007; Boswell, 2009). Gas hydrate is an ice-like solid compound formed of water molecules clustered around methane molecules that is stable under high pressure and low temperature conditions, commonly found in permafrost settings and submarine sediments (Milkov & Sassen, 2002; Sloan, 2003; Makogon et al., 2007; Rutqvist & Moridis, 2007; Sloan & Koh, 2008; Makogon, 2010; Collett et al., 2011). Thermodynamic perturbations that lead to the dissociation of GHBS release large amounts of methane gas and free liquid water (Englezos, 1993; Sloan & Koh, 2008; Haligva et al., 2010; Collett et al., 2015), which in turn trigger significant changes in fluid pressure and in sediment effective stress (Sánchez et al., 2017). Furthermore, gas hydrate dissociation is an endothermic process that tends to absorb heat from the surroundings, while gas hydrate formation is exothermic. To properly simulate such strongly coupled thermo-hydro-chemo-mechanical (THCM) processes involving GHBS, it is critical to have a formal approach able to account for the multiphysical interactions triggered by gas hydrate dissociation and/or formation.

Equilibrium and kinetic reaction models are the two primary approaches commonly used to simulate processes of gas hydrate formation and dissociation. Equilibrium models assume that gas hydrate phase changes take place instantaneously upon perturbations in thermodynamic conditions that bring GHBS out of the stability zone. In contrast, kinetic models consider that gas hydrate does not immediately dissociate upon changes in pressure-temperature (*P*-*T*) conditions, but that phase changes take place over time. Kowalsky & Moridis (2007) conducted numerical simulations involving full-scale GHBS reservoirs undergoing gas hydrate dissociation via depressurization and/or heating using both, equilibrium and kinetic reaction models. Results were comparable when considering long-term results, i.e. under steady-state conditions; however, transient analyses showed significant differences between the two types of model. Moreover, when simulating short-term problems, such as dissociation tests involving gas hydrate bearing cores, equilibrium models are not able to provide reliable predictions (Gamwo & Liu, 2010).

Kim et al. (1987) conducted a series of methane hydrate dissociation tests under controlled conditions in the laboratory, investigating depressurization at different (constant) temperatures and the effect of pressure gradient on the rate of dissociation. These results formed the basis of a kinetic reaction model for methane hydrate dissociation that is a function of the kinetic constant, the reaction surface area, and the fugacity of methane under local pressure and temperature (Kim et al., 1987). The kinetic constant depends on the activation energy, local temperature, and the intrinsic kinetic constant, which should be measured for gas hydrate dissociation (Clarke & Bishnoi, 2000, 2001) and formation (Englezos et al., 1987a,b). The kinetic reaction model has been widely used and calibrated in the literature (Jamaludin et al., 1989;

Rempel & Buffett 1997, 1998; Ahmadi et al., 2004; Pooladi-Darvish, 2004; Kneafsey et al., 2005, 2007; Nazridoust & Ahmadi, 2007; Kwon et al., 2008; Fang, 2009; Gamwo & Liu, 2010; Liang et al., 2010; Kimoto et al., 2007, 2010; Ruan et al., 2012; Cheng et al., 2013; Moridis 2014; Gupta et al., 2015; Chen et al., 2017; Sun et al., 2018; De La Fuente et al., 2019). Despite being a popular approach, the kinetic reaction model has some drawbacks. It depends on a large number of parameters and some are not easy to directly obtain. For example, the determination of the reaction surface area (i.e. the interface area between gas hydrate and surrounding phases) remains contentious, as discussed in Sun & Mohanty (2006). Various equations have been suggested for estimating this parameter (Yousif et al., 1991; Masuda et al., 2002; Moridis et al., 2005; Sun & Mohanty, 2006), but there is no consensus as to the most appropriate formulation. The computational cost is another disadvantage of this model (Kowalsky & Moridis, 2007). Yin et al. (2016) discuss uncertainties related to the mechanisms behind the kinetic behavior of gas hydrate, which result in inaccurate determination of activation energy and the intrinsic kinetic constant.

The objective of this paper is to propose a simple alternative approach to the numerical simulation of methane hydrate phase changes in GHBS. Our new approach, hereafter referred to as a pseudo-kinetic model, revisits the experimental observations of Kim et al. (1987) and is formulated in the *P*-*T* plane. The model involves one parameter only that controls the rate of gas hydrate dissociation and is easy to calibrate from experimental data. We show that our model is able to simulate the time dependent behavior of methane hydrate during its dissociation and formation, and is also applicable to liquid-water to ice phase transitions. We first present some basic relationships and concepts related to phase transformations in GHBS, and outline the kinetic model of Kim et al. (1987). We describe the full mathematical formulation of the new pseudo-kinetic model together with its implementation in a fully coupled THCM finite element program recently proposed to model problems involving GHBS (Sánchez et al., 2018). We validate the model against the experimental results of Kim et al. (1987). We then evaluate the model against a series of different cases involving methane hydrate dissociation/formation and ice formation/thawing. Our findings support the suitability of our simpler pseudo-kinetic model to tackle the multiple phase transformations typically present in short- and long-term analyses involving GHBS.

2. Gas Hydrate Bearing Sediments Phases and Phase Changes

GHBS are composed of five main phases (Figure 1): solid (*s*); liquid (*l*); gas (*g*); hydrate (*h*); and ice (*i*). As hydrate and ice are solid compounds that (depending on thermodynamic conditions) can disappear during the analysis, volumes related to these two phases, together with the V_g and V_l, comprise the volume of voids (i.e. $V_v = \Sigma V_\beta$, where β: ℓ, *g*, *h*, *i*). The sum of the volume of voids plus the volume of solid (i.e. $V_{total} = V_v + V_s$) yields the total volume V_{total} of the sediment. Based on these definitions, the total porosity can be calculated as:

$$\phi = \frac{1 - V_s}{V_{total}} = \frac{V_v}{V_{total}} \quad (1)$$

The volume fractions relate to four potential phases, which occupy the volume of voids, defined as $S_\beta = V_\beta / V_v$ and subjected to the restriction below:

$$S_l + S_g + S_h + S_i = 1 \quad (2)$$

Furthermore, the effective pore space (V_v^*) is defined as the portion of void space occupied only by the fluid phases (i.e. *l* and *g*, where $V_v^* = V_l + V_g$). Effective saturations, which relate to the liquid ($S_l^* = V_l / V_v^*$) and gas ($S_g^* = V_g / V_v^*$) phases, can also be defined.

Three main species make up the phases of GHBS (Figure 1b): mineral; water (*w*); and methane (*m*). Mineral is the only component of the solid phase. Water is the main component of the liquid phase, the only component of the ice phase, is present in the hydrate phase (i.e. in an ice-like structure), and can be found in the gas phase (as water vapor). Methane is the main component of the gas phase, is also present in the liquid phase (as a dissolved gas), and in the hydrate phase (i.e. as an ice-like compound).

Gas hydrate formation/dissociation and ice formation/thawing are the most relevant phase transformations that control the behavior of GHBS. In the following, we discuss the phase boundaries in *P*-*T* space delimiting the stable states of the different phases typically encountered in methane hydrate. We then present the proposed pseudo-kinetic approach and its capacity to deal with unstable conditions and the corresponding phase transitions.

2.1. Phase boundaries

The equation below expresses the methane hydrate phase boundary, which defines the hydrate stability zone in the *P*-*T* space (Sloan & Koh, 2008):

$$P_{eq-h} = e^{\left(40.234 - \frac{8860}{T_{eq-h} - \alpha_s I_s}\right)} \quad (3)$$

where $P_{eq\text{-}h}$ [kPa] and $T_{eq\text{-}h}$ [K] are the equilibrium pressure and temperature, respectively. Water salinity also affects the gas hydrate phase boundary (e.g. Kamath & Godbole, 1987). Equation (3) considers this effect both through the water salinity I_s (expressed in terms of the salt concentration, in weight), and the parameter α_s (which corresponds to the slope of the temperature-salinity curve). Based on Equation (3), the green solid line in Figure 2 represents the methane hydrate phase boundary in the case of pure water.

The ice/liquid-water phase boundary can also be written in terms of pressure and temperature (Wagner & Kretzschmar, 2008):

$$P_{eq-i} = 13.0\left(273.16 - T_{eq-i}\right) \quad (4)$$

where $P_{eq\text{-}i}$ [MPa] and $T_{eq\text{-}i}$ [K] use the definitions above, for the case of methane hydrate (i.e. $P_{eq\text{-}h}$ and $T_{eq\text{-}h}$) but in relation to the ice phase boundary.

According to Figure 2, four regions emerge when the methane hydrate stability (solid line) and the ice/liquid-water (dashed line) phase boundaries are superimposed on the *P-T* space. The ice phase is stable on the left side of ice/liquid-water phase boundary. Therefore, ice transforms into liquid in Zone A, whereas ice forms by freezing of liquid water in Zones C and D. Likewise, methane hydrate is stable in Zones B and D, located above the corresponding phase boundary. If during the analysis the *P-T* path is such that it brings methane hydrate out of the stability regions (i.e. Zones A or C), it will be in an unstable condition with a tendency to dissociate into gas and liquid. Note that the liquid phase is also unstable in Zone C and therefore, after hydrate dissociation, will transform into ice. In Zone B, the coexistence of both liquid and gas phases results in hydrate formation until one vanishes. A *P-T* path that moves from Zones A to D may lead to the presence of both liquid and gas phases in the hydrate and ice stability zones. Depending on the rate of gas hydrate formation and ice freezing, a portion of liquid is consumed with the available gas phase to form hydrate and the remainder will freeze. Similarly, if both, ice and gas phases exist in Zone D and a variation in the *P-T* path causes a shift to Zone B, the liquid phase, which resulted from melting in the unstable ice phase, is consumed with the gas phase to form hydrate.

Thus, any stimulus that places a phase in the unstable zone (e.g. the occurrence of hydrate below its phase boundary or the existence of liquid on the left side of ice/liquid-water phase boundary) will result in a phase transition.

2.2. Kinetic model of Kim et al. (1987)

Kim et al. (1987) proposed a kinetic model that considers the rate of gas hydrate dissociation inherently as a function of pressure, temperature, and surface area of gas hydrate, as follows:

$$-\frac{dn_h}{dt} = k_d A_S \left(f_e - f\right) \quad (5)$$

where n_h indicates the total moles of methane contained in the methane hydrate; A_S is the methane hydrate surface area; (f_e-f) is the driving force defined as the difference between the fugacity of methane at the equilibrium pressure and that of methane at the solid surface (i.e. assumed as the fugacity of methane in

the bulk gas phase) both at the corresponding temperature; and k_d is the kinetic constant written as an Arrhenius-type equation:

$$k_d = k_{d0} \exp\left(-\frac{\Delta E_a}{RT}\right) \quad (6)$$

where k_{d0}, ΔE_a, and R are the intrinsic kinetic constant, the activation energy, and the gas constant, respectively. Equation (5) requires the surface reaction area, and different models have been proposed to estimate it (e.g. Yousif et al., 1991; Masuda et al., 2002; Moridis et al., 2005; Sun & Mohanty, 2006). These models generally involve additional parameters and the inclusion of S_h in the calculation of the surface reaction area. Numerical codes are generally formulated in terms of pressures and saturations, therefore additional calculations are usually necessary to obtain the fugacity.

3. *Proposed Pseudo-Kinetic Model*

We revisited the experimental tests reported in Kim et al. (1987) to investigate the effect of temperature, fluid pressure changes, and current *P-T* condition, on the rate of hydrate dissociation, with the aim of proposing a simpler model to simulate methane hydrate dissociation. Kim et al. (1987) performed a set of experiments where they injected ultra-high pure methane into a container with 300cm^3 of double distilled and de-ionized water at favorable pressure and temperature to form 9cm^3 of methane hydrate (i.e. $S_h \sim$ 0.03). They reported the time required to achieve (full) hydrate dissociation in several experiments where the specimens were subjected to different pressure gradients, applied at different constant temperatures. Figure 3a illustrates these results for two different temperatures subjected to three different pressure gradients. The gas hydrate was depressurized from a pressure slightly above the corresponding equilibrium value up to different target values (i.e. shown by circle, square, and triangle symbols, in a decreasing manner, respectively). Figure 3b presents the corresponding times to achieve the full hydrate dissociation. In the second set of experiments, the depressurization and associated dissociation of two samples was induced at two constant temperatures, 279.2K (Series_3) and 283.3K (Series_4). In both cases, the pressure decreased from a value slightly above the corresponding equilibrium pressure until it reached the target final pressure around 2.69MPa (Figure 4a). Figure 4b presents the results of tracking the time evolution of hydrate concentration during dissociation, in terms of hydrate saturation.

Our pseudo-kinetic model for GHBS assumes that the rate of gas hydrate dissociation depends on the distance between the phase boundary and the current (unstable) *P-T* state (induced by changes in pressure, and/or temperature, and/or water chemistry), and that phase transformation becomes faster as this distance increases. This approach is consistent with the dissociation experiments reported by Kim et al. (1987), which show that the further the applied pressure from the phase boundary (i.e. larger pressure gradients),

the faster the same amount of methane hydrate dissociates, as shown in Figure 3 (Series_1 vs Series_2). Moreover, according to Figure 4, the rate of methane hydrate dissociation is lower in test Series_3 than in Series_4 (in which the *P*-*T* state is further from the phase boundary). In this context, we propose that the rate of methane hydrate dissociation, Γ_h (Sec^{-1}), is given by:

$$\Gamma_h = \frac{1 - q_{hd}^{\ \delta_h}}{t_1} \tag{7}$$

where t_1 is the unit of time, q_{hd} is a model parameter (where $0 < q_{hd} < 1$) calibrated from gas hydrate dissociation tests (see Section 5.1); and $\underline{\delta}_h$ is a measure of the distance between the current *P*-*T* state and the phase boundary, calculated as:

$$\delta_h = \sqrt{\left[\delta_T \left(T - T_{eq}\right)\right]^2 + \left[\delta_P \left(P - P_{eq}\right)\right]^2} \tag{8}$$

where δ_T (K^{-1}) and δ_P (MPa^{-1}) are scaling parameters (i.e. equal to $1K^{-1}$ and $1MPa^{-1}$, respectively). It is apparent that δ_h is the non-dimensional expression of the actual chord on the phase boundary ($\underline{\delta}$, Figure 5) associated with an unstable *P*-*T* state. For example, consider a case in which a thermodynamic change in the sediment brings methane hydrate to a point *P*-*T* in the Zone A, where it is unstable. The associated $P_{eq\text{-}h}$ and $T_{eq\text{-}h}$ related to the new *P*-*T* condition can be determined from the methane hydrate phase boundary (Equation 3). From Equations (8) and (7), we obtain the rate of gas hydrate dissociation. It is evident that as the distance increases between the phase diagram and the *P*-*T* point (which defines the current state), the cord increases and consequently methane hydrate dissociates faster. A similar approach is followed for modeling gas hydrate formation, using the same constant (i.e. $q_{hd} = q_{hf} = q_h$). However the proposed approach allows us to consider different rates for formation and dissociation by adopting different parameters for each phase transformation process.

In similar fashion, the rate of ice/liquid-water phase transition Γ_i can be obtained from:

$$\Gamma_i = \frac{1 - q_i^{\ \delta_i}}{t_1} \tag{9}$$

where q_i is a model parameter (where $0 < q_i < 1$) that can be calibrated from ice thawing/formation experiments; and $\underline{\delta}_i$ is like $\underline{\delta}_h$, which is calculated similar to Equation (8) but in terms of $P_{eq\text{-}i}$ and $T_{eq\text{-}I}$ (i.e. related to the ice/liquid-water phase boundary, calculated from Equation 4). To illustrate how the proposed model works, in the following sections we explain in more detail cases related to gas hydrate dissociation/formation and ice formation/thawing.

3.1. Gas hydrate dissociation

Consider an initial gas hydrate saturation (S_h^i) that is brought outside the stability zone by a perturbation (i.e. Zones A and C on the *P-T* space). Hydrate saturation reduces during dissociation and we assume that the amount relates to the distance to the phase boundary (estimated from Equation 8). The rate of decreases in gas hydrate saturation, $\dot{S}_h$ (Sec^{-1}) can be calculated from Equation (7), such that:

$$\dot{S}_h = -\Gamma_h \tag{10}$$

The updated gas hydrate saturation S_h^{i+1} can be obtained as follows:

$$S_h^{i+1} = S_h^i - \Gamma_h dt \tag{11}$$

where the superscript (*i*) and (*i+1*) represent the previous and current time-steps, respectively, the subscript indicates the phase, and *dt* is the time-step interval (i.e. from *i* to *i+1*).

The liquid and gas phases share the effective void space of the GHBS. The distribution between them is dictated by the capillary pressure (i.e. $P_c = P_g - P_l$) through the capillary pressure (or water retention) curve of the sediment. Different capillary pressure curves have been proposed. For example, if the van Genuchten (1978) model is chosen to estimate the portion of the effective void space that is occupied by the liquid phase, the following expression may be used:

$$S_\ell^* = \frac{S_\ell}{S_\ell + S_g} = \left[1 + \left(\frac{P_c}{P_o}\right)^{\frac{1}{1-m}}\right]^{-m} \tag{12}$$

where P_o is a model parameter associated with the breakthrough gas pressure, and *m* is a parameter that controls the imbibition rate (typically $0.05 < m < 0.4$). More recently, an updated Brooks and Corey (1964) capillary pressure model examines the presence of gas hydrate in the pore space (Gupta et al., 2015):

$$S_\ell^* = \frac{S_\ell}{S_\ell + S_g} = \left[\frac{P_c}{P_o f_{Sh} f_\phi}\right]^{-m_{bc}} \tag{13}$$

where m_{bc} is a sediment parameter, f_{sh} and f_Φ represent the scaling parameters that depend on hydrate saturation (Clement et al., 1996; Rockhold et al., 2002) and porosity (Civan, 2000), respectively, as follows:

$$f_{sh} = \left(1 - S_h\right)^{\frac{C_1 m_{bc} - 1}{C_1 m_{bc}}} \tag{14}$$

$$f_\phi = \frac{\phi_0}{\phi}\left(\frac{1-\phi}{1-\phi_0}\right)^{C_2} \quad (15)$$

where ϕ_0 is the reference porosity; C_1 and C_2 are model parameters.

Regardless of the adopted capillary pressure model (i.e. Equations 12, or 13, or any alternative), the updated S_l and S_g accounting for hydrate dissociation are derived as follows;

$$S_l = S_l^*\left[1-\left(S_h + S_i\right)\right] \quad (16)$$

$$S_g = \left(1-S_l^*\right)\left[1-\left(S_h + S_i\right)\right] \quad (17)$$

where $[1-(S_h+S_i)]$ defines the effective void volume. Note that Equations (16) and (17) correspond to the case of hydrate dissociation lying in Zone A. If during hydrate dissociation, the *P-T* state is in Zone C, the water released during this process will form ice, since liquid water is unstable in this zone. Therefore, the calculated values in Equation (16) and (17) are not the final values for liquid and gas saturations, because the phase transitions based on the ice/liquid-water phase boundary need to be considered, as detailed below (Section 3.3).

3.2. Gas hydrate formation

Methane hydrate is stable in Zones B and D (Figure 2). Furthermore, if both, methane gas and liquid water are available under the *P-T* conditions that prevail in Zone B, methane hydrate will form. Hydrate formation leads to a decrease of the partial void volume occupied by fluid phases (i.e. *l* and *g*). There are two possible cases for this phase transformation, with hydrate formation controlled by either, excess water, or excess methane. In the first case, for an existent mass of methane, the water available is higher than (or equal to) the required mass to form hydrate; in the second case (i.e. excess methane), the available mass of methane is higher than that required to from hydrate with the available water in the pore space. The variable δ' defined below is used to assess whether the current condition corresponds to a case with excess methane or excess water:

$$\begin{cases} \dfrac{\rho_l S_l^i}{\rho_g S_g^i} \geq \left(\delta' = \dfrac{\alpha}{1-\alpha}\right) \rightarrow excess\ \ water \\ \dfrac{\rho_l S_l^i}{\rho_g S_g^i} < \left(\delta' = \dfrac{\alpha}{1-\alpha}\right) \rightarrow excess\ \ methane \end{cases} \quad (18)$$

where ρ_g and ρ_l are the gas and liquid phase densities, respectively; and a is the water mass fraction in the gas hydrate solid compound. In the case of methane with structure-I, a=0.866.

Therefore, for the excess methane case, the phase saturations can be updated according to:

$$S_h^{i+1} = S_h^i + \Gamma_h \left(\frac{\rho_l}{\alpha \rho_h} \right) dt \quad (19)$$

where ρ_h stands for hydrate phase density and $\Gamma_h[\rho_l/(\alpha\rho_h)]$ corresponds to the rate of gas hydrate formation (i.e. $\dot{S}_h$) for the case of phase change under excess methane.

For the case of excess water, a similar procedure is followed:

$$S_h^{i+1} = S_h^i + \Gamma_h \left(\frac{\rho_g}{(1-\alpha)\rho_h} \right) dt \quad (20)$$

where $\Gamma_h[\rho_g/([1-\alpha]\rho_h)]$ corresponds to the rate of gas hydrate formation (i.e. $\dot{S}_h$) for the case of a phase change under excess water. Furthermore, liquid and gas saturations are updated, as discussed, using Equations (16) and (17). If the *P*-*T* path is located in Zone D, the updated liquid saturation is also subject to ice formation.

3.3. Ice formation

Liquid water under *P*-*T* conditions prevailing in Zones C or D freezes. The corresponding ice saturation can be updated according to:

$$S_i^{i+1} = S_i^i + \Gamma_i \left(\frac{\rho_l}{\rho_i} \right) dt \quad (21)$$

where $\Gamma_i[\rho_l/\rho_i]$ represents the rate of ice formation (i.e. $\dot{S}_i$).

3.4. Ice thawing

Under the *P*-*T* conditions that prevail in Zones A and B, ice melts and leads to an increment in the liquid phase. Therefore, the ice saturation is updated as follows:

$$S_i^{i+1} = S_i^i - \Gamma_i dt \quad (22)$$

where Γ_i represents the rate of ice thawing (i.e. $\dot{S}_i$). After considering the variation in S_i, the effective void volume is updated and the liquid and gas saturations are updated using Equations (16) and (17). We assume that all water freezes under freezing conditions; however, the presence of unfrozen water in

frozen sediments (e.g. Taber, 1929) can be easily included in the formulation. In all cases discussed above, a minimum (residual) saturation associated with each of the different phases can be defined.

4. *Pseudo-Kinetic Model Implementation in Multiphysical Finite Element Framework*

The pseudo-kinetic model discussed above was implemented in the finite element program CODE_BRIGHT (Olivella et al., 1996), recently upgraded by Sánchez et al. (2018) to deal with coupled THCM processes involving GHBS. To describe the behavior of GHBS, we consider a set of equations: balance equations (with the associated main unknowns being liquid and gas pressures, temperatures, and displacements); constitutive equations (with the corresponding dependent variables including heat and phases fluxes, partial phase saturations, porosity, and stresses); equilibrium restrictions, and phase transformation equations. The key THCM processes anticipated in GHBS are: i) methane and water flow driven by advective and non-advective flows; ii) heat transfer via conduction and phase advection; iii) heat of phase transformation (i.e. methane hydrate dissociation/formation and ice thawing/formation); iv) deformable sediment. Below we present a brief summary of the main components of the adopted formulation, full details can be found in Sánchez et al. (2018).

4.1. *Balance equations*

The gas and liquid pressures, porosity, temperature, and sediment displacements are the main unknowns adopted, and solved by methane mass, water mass, mineral mass, internal energy, and momentum balance equations, respectively.

Methane mass balance equation:

$$\frac{\partial}{\partial t}\underbrace{\left\{\left[\theta_g^m S_g+\theta_\ell^m S_\ell+(1-\alpha)\rho_h S_h\right]\phi\right\}}_{\text{mass methane per unit volume}}+\nabla.\underbrace{[\mathbf{j}_g^m+\mathbf{j}_l^m+(1-\alpha)\rho_h S_h\phi\mathbf{v}]}_{\text{flux methane in gas; liquid; and hydrate}}=f_e^m \tag{23}$$

where θ_g^m and θ_l^m are the mass fraction of methane per unit volume of gas and liquid phases, respectively; $\boldsymbol{j}_l^m$ and $\boldsymbol{j}_g^m$ are the motion of methane in the liquid and gas phases with respect to the fixed reference system (which are obtained as the sum of non-advective and the advective fluxes); velocity $\boldsymbol{v}$ of the solid phase relative to the fixed reference frame; and f_e^m is the external sink/source of methane per unit volume. The first term (left hand side) considers the mass exchange of methane during the relevant phase transitions (i.e. hydrate formation/dissociation for the case of methane). Moreover, we assume that the hydrate phase moves with the solid particles (the last term on the left-hand side). The proposed framework is also able to account for the non-advective diffusive transport of species in the phases (i.e. *w* in *g*, and *m* in *l*) (Sánchez et al., 2018).

Water mass balance equation:

332 The water mass balance is derived in a similar manner as follows:

$$\frac{\partial}{\partial t}\underbrace{\left\{\left[\theta_g^w S_g+\theta_\ell^w S_\ell+\alpha\rho_h S_h+\rho_i S_i\right]\phi\right\}}_{\text{mass water per unit volume}}+\nabla.[\underbrace{\mathbf{j}_g^w+\mathbf{j}_l^w+\alpha\rho_h S_h\phi\mathbf{v}+\rho_i S_i\phi\mathbf{v}}_{\text{flux water in gas; liquid; hydrate; and ice}}]=f_e^w \tag{24}$$

333 where superscript *w* indicates the water species and ρ_i stands for ice phase density.

334 *Mineral mass balance equation*:

335 Minerals only occur as solid particles. The mass balance equation follows:

$$\frac{\partial}{\partial t}\underbrace{[\rho_s(1-\phi)]}_{\substack{\text{mass mineral}\\ \text{per unit volume}}}+\nabla\cdot\underbrace{[\rho_s(1-\phi)\mathbf{v}]}_{\text{mineral in solid}}=0 \tag{25}$$

336 where ρ_s is the density of the solid particles.

337 *Internal energy balance equation:*

$$\begin{aligned}&\frac{\partial}{\partial t}\underbrace{\left\{\left[e_s\rho_s(1-\phi)\right]+\left(e_\ell\rho_\ell S_\ell+e_g\rho_g S_g+e_h\rho_h S_h+e_i\rho_i S_i\right)\phi\right\}}_{\text{energy per unit volume of the hydrate bearing sediment}}\\ &+\nabla.[\ \underbrace{\mathbf{i}_c+\left(\mathbf{j}_{El}+\mathbf{j}_{Eg}+\mathbf{j}_{Eh}+\mathbf{j}_{Ei}+\mathbf{j}_{Es}\right)}_{\text{heat conduction+heat transport in phases } \ell,\ g,\ h,\ i,\ s}\ ]=f^E\end{aligned} \tag{26}$$

338

339 where e_β is the specific internal energy per unit mass of each phase (listed in Table 1); $\boldsymbol{i}_c$ is the flux
340 associated with the heat conduction through GHBS; $\boldsymbol{j}_{E\beta}$ is the total heat transport related to the phases (β)
341 movement (including advective and non-advective fluid fluxes relative to the mineral skeleton plus the
342 motion of whole sediment with respect to a fixed reference system); f^E is the energy supply per unit
343 volume of GHBS (Sánchez et al., 2018).

344 We assume thermal equilibrium amongst the phases. Energy consumption or liberation associated with
345 gas hydrate formation/dissociation and ice formation/fusion are taken into consideration by the
346 corresponding latent heats or changes in enthalpy. Furthermore, the balance equation inherently captures
347 energy changes during endothermic or exothermic processes through specific internal energies and the
348 corresponding changes in volume fractions.

349 *Momentum balance equation*

$$\nabla.\boldsymbol{\sigma}_t+\mathbf{b}=0 \tag{27}$$

where $\boldsymbol{\sigma}_t$ is the total stress tensor and $\boldsymbol{b}$ is the body forces vector. We have assumed the absence of inertial forces (i.e. quasi-static problems).

4.2. Constitutive equations

Constitutive equations allow us to relate unknowns to dependable variables and to rewrite the equilibrium equations as a function of the main unknowns. Likewise, the constitutive equations capture coupling among the various phenomena incorporated in the formulation.

The proposed framework considers simple yet robust constitutive laws. For example, we assume that the Fourier's law describes heat fluxes,

$$\mathbf{i}_c = -\lambda_{hbs} \nabla T \tag{28}$$

where λ_{hbs} is the thermal conductivity of the GHBS. A non-linear volume average model is selected to track the evolution of λ_{hbs} during the simulation,

$$\lambda_{hbs} = \left[(1-\phi)\lambda_s^{\beta'} + \phi\left(S_h \lambda_h^{\beta'} + S_i \lambda_i^{\beta'} + S_g \lambda_g^{\beta'} + S_\ell \lambda_\ell^{\beta'} \right) \right]^{\frac{1}{\beta'}} \tag{29}$$

where λ_β is the thermal conductivity of each phase derived (i.e. λ_l = 0.58, λ_g = 0.01, λ_i = 2.1, λ_h = 0.5, λ_s = 5.0Wm^{-1}K^{-1}; Sánchez & Santamarina, 2016). This law reduces to the parallel and series models when β'=1 and β'=-1, respectively. As reported in Santamaria & Ruppel (2008), an adequate prediction for different conditions is obtained with $\beta' \approx -0.2$.

We also assume that the generalized form of Darcy's law governs advective fluid fluxes:

$$\mathbf{q}_\beta = -\mathbf{K}_\beta \left(\nabla P_\beta - \rho_\beta \mathbf{g} \right); \qquad \beta = \ell, g \tag{30}$$

where $\mathbf{g}$ is the gravity vector (i.e. the scalar g=9.8m/s^2 times the vector $[0,0,1]^T$), and $\mathbf{K}$ is the hydraulic conductivity tensor (calculated from Equations T2.1 to T2.3 in Table 2).

Different options are available to model the mechanical behavior of GHBS (e.g. Klar et al., 2010; Santamarina & Rupple, 2010; Uchida, et al., 2012; Gai et al., 2107; Sánchez et al., 2017). Here we adopt the simple elastic model that includes the dependence of Young's modulus on hydrate saturation (Santamarina & Rupple, 2010):

$$E_{Sh} = \left[E_{Sed} + dE_{Sed} (\phi_0 - \phi) \right] \left(\sigma_C / \sigma_{C0} \right)^b + cE_{Hyd} (S_h)^d \tag{31}$$

where E_{Sh} , E_{Sed} , and E_{Hyd} are respectively Young's modulus of GHBS, of hydrate-free sediments (at the reference porosity ϕ_0 and confining stress of σ_{C0} =1KPa) and of pure gas hydrate; dE_{Sed} accounts for the dependence of E_{Sed} on ϕ_0; b, c, and d control the sensitivity of E_{Sed} on the confining stress σ_C.

In addition to the above equations, and the retention curve presented in Equations (12) and (13), Table 2 summarizes the other essential constitutive equations.

5. Model Applications

In this Section we apply the new model to solve different problems, as follows. In Section 5.1 we validate the pseudo-kinetic model by comparing the experimental results of the tests conducted on synthetic gas hydrate samples reported by Kim et al. (1987), with the outputs of models replicating these tests conditions. Section 5.2 is related to the evaluation of the model considering *P-T* paths that covered a variety of phase transformations. The model validation reported in Section 5.3 compares model and experimental results from a scaled gas production test on a natural GHBS specimen. In Section 5.4 we evaluate the model performance for long term conditions associated with the gas hydrate and ice formation in the permafrost. The application cases cover both short (hours) and long ($2x10^6$ years) timescales.

5.1. Pseudo-kinetic model validation

To validate the proposed pseudo-kinetic model, we use the experimental results reported in Kim et al. (1987) and described above (Figures 3 and 4). Our numerical models attempt to reproduce the test set-up based on the initial conditions (i.e. S_h = 0.03 and S_l = 0.97) and the evolution of pressure at the imposed constant temperatures (Kim et al., 1987). The first set of experiments (Figure 3) were carried out at two different constant temperatures (T = 274.2K; and T = 279.0K) to investigate the effects of pressure gradient (i.e. ΔP respect to $P_{eq\text{-}h}$) on hydrate dissociation time. Figure 6 shows the experimental times required to achieve full hydrate dissociation for each depressurization experiment, together with the corresponding times computed with our model for those tests. According to Kim et al. (1987), the slight scatter observed in the experimental results is associated with small temperature changes during hydrate dissociation (some experiments were discarded due to experimental problems). The pseudo-kinetic model is able to satisfactorily capture both the effect of pressure-gradient and temperature on the final hydrate dissociation time.

In the second set of experimental results from Kim et al. (1987) (Figure 4) the time evolution of hydrate dissociation was reported at two different constant temperatures (T = 279.2K and T = 283.3K). The experimental results are shown in Figure 7 together with our model results (from Equation 11). The

pseudo-kinetic model captures the differences in hydrate dissociation rates observed in these experiments. It performs particularly well at the beginning of the tests but exhibits a slight discrepancy between simulations and experiments at low saturations for T = 279.2K (Series_3). The dashed lines in Figure 7 show additional model results based on a slight variation of Equation (11) to account for the apparent dependence of gas hydrate dissociation rate on hydrate saturation. The modified law is:

$$S_h^{i+1} = S_h^i \left(1 - \Gamma_h dt\right) \tag{32}$$

The revised model closely captures the non-linear behavior observed in the experiments, and can be useful for those cases in which a precise modeling of gas hydrate dissociation is required at low S_h. However, our aim here is not to perfectly match these experiments, but to show the flexibility of the proposed approach to capture complex features of gas hydrate dissociation. Alternative equations can be proposed as required based on the proposed framework. The model results presented in Figures 6 and 7 were obtained with a q_{hd}=0.999 (Equation 7). This constant together with Equations (7) and (11) are used in all the simulations presented in the following sections.

5.2. Model evaluation using synthetic cases

Having validated the pseudo-kinetic model, we propose a number of synthetic cases to evaluate its ability to deal with different *P-T* paths that involve phase transformations. We assume sediment placed within a chamber where different initial and boundary conditions can be controlled. The synthetic cases are solved at point level (i.e. at gauss integration level in the context of a finite element code), by imposing controlled changes of fluid pressures and/or temperature. This type of analysis is important because it allows checks on the algorithm used at local (element) level during the numerical integration. The initial porosity of the specimen is $\phi = 0.33$ and the intrinsic (isotropic) permeability $k_0 = 1.0\text{x}10^{-12}\text{m}^2$ (at ϕ_0). Equation (29) controls the thermal conductivity with $\beta' = -0.2$. Parameters $P_0 = 0.1$MPa, and $m = 0.5$ are adopted for the capillary curve (Equation 12). We assume a poroelastic sediment according to Equation (31), with $E_{Hyd} = 1.35$GPa, $E_{Sed} = 0.03$GPa, $b = 0$, $c = 1$, and $d = 1$. The selected cases cover different initial phase saturations and *P-T* trajectories, as described below.

First, we simulate two cases of hydrate dissociation by depressurization from an initial sediment (lying in stability Zone B) until atmospheric pressure stabilizes. As this is a point level analysis, the gas is ejected just after hydrate dissociation, therefore the capillary pressure remains close to zero. Case I involves an initial pressure and temperature of $P_i = 13$MPa and $T_i = 287.65$K, with initial saturations of $S_{hi} = 0.25$ and $S_{li} = 0.75$, under excess water conditions. We assume an adiabatic system (i.e. there is no heat exchange between the vessel containing the sediment and the surroundings). Figure 8a presents the initial *P-T* conditions and saturations and their changes during the hydrate dissociation process for Case I. The *P-T*

trajectory moves vertically down to meet and then follow the phase boundary. The temperature reduces during hydrate dissociation due to the endothermic character of the reaction. At T_f = 274.69K all hydrate dissociates, the *P-T* path leaves the phase boundary, and pressure decreases until P_f = 0.1MPa with no variations in sediment temperature. Case II assumes an initially cooler sediment, T_i = 277.15K (Figure 8b). During hydrate dissociation under these conditions, the *P-T* path crosses the ice/liquid-water phase boundary and liquid water freezes with a corresponding increase of S_i and decrease of S_l. The ice/liquid-water phase change is exothermic and heating assists the hydrate dissociation and impacts the S_h slope in the *P-T* plane. Upon completing hydrate dissociation, the cooling associated with this reaction finishes. Heating associated with ice formation warms the sediment, the *P-T* path leaves the hydrate phase boundary and follows the ice/liquid-water phase boundary, finishing at atmospheric pressure and a final temperature of T_f ~ 272.5K.

These results show that the proposed approach is able to deal with the complex interactions and phase changes associated with the synthetic cases. It is worth mentioning that the same type of behavior in the *P-T* plane was observed in a depressurization test conducted under controlled conditions on a natural methane hydrate bearing core from the Krishna Godavari Basin (Yun et al., 2010).

We also consider two cases involving hydrate formation with trajectories from Zones A to B. Case III involves hydrate formation starting with the following initial pressure and temperature: P_i = 15MPa and T_i = 293.15K. We assume an initial stress σ_0 = 15MPa. Hydrate forms by cooling the sediment to a final temperature T_f = 275.15K, while impermeable boundaries are assumed, so that pore pressure is not constant during the experiment. An excess water condition is assumed considering initial saturations for the liquid and gas phases equal to 0.5 (i.e. $S_l = S_g$ = 0.50). Hydrate starts to form when the *P-T* path meets the hydrate phase boundary (Figure 9a), and continue forming progressively as the trajectory follows the phase boundary until all available methane gas is consumed. A decrease of the fluid pressure takes place during this process, from P_i = 15MPa to P_f = 8.73MPa. Under these conditions, the final saturations are: S_h ~ 0.42 and S_l ~ 0.58.

In Case IV the initial conditions and saturations are similar to Case III, but pore pressure is kept constant during the experiment (i.e. pure water and/or methane could enter or leave the vessel to ensure that the liquid and/or gas pressure remains constant). Figure 9b presents the initial *P-T* conditions, phase saturations, and their changes during the formation process for Case IV. Hydrate formation occurs when the *P-T* path crosses the phase boundary (i.e. moving from Zones A to B), hydrate forms at this point consuming all available methane. Cooling continues afterwards without phase transformations, with saturations of S_h ~ 0.30 and S_l ~ 0.70. In Case IV effective stresses remain constant (i.e. no changes in pore pressure) and therefore porosity does not change during the test. However, in Case III, the sediment

contracts (i.e. $\phi_f \sim 0.21$), because the effective stresses increase with the specimen depressurization that takes place during hydrate formation.

5.3. Modeling a dissociation test from a gas hydrate bearing core

To further validate the pseudo-kinetic model, we simulate a dissociation experiment involving natural GHBS. The specimen was acquired from the Ulleung Basin using the instrumented pressure testing chamber (IPTC), which maintained a good quality specimen at 4°C and 15MPa (Yun et al., 2011). A specimen 822mm length and 50mm diameter was subsampled under pressure to simulate depressurization induced gas production (Yun et al., 2011). Table 3 lists the index properties of this sediment.

Figure 10 illustrates the IPTC containing the GHBS, the ball-valve, and the thermocouple. Controlled depressurization of the core involved a gradual reduction of hydrostatic pressure at an average rate of 0.146MPa/min for 50min, until it reached the methane hydrate stability phase boundary. This rate was reduced afterwards, and maintained for 130min at ~ 0.0115MPa/min, until reaching P = 3.2MPa. The valve was then closed for around 8hours (from t = 180min to t = 650min), during which time the temperature remained constant at 1.2°C, while there was a slight rebound in pressure from 3.2MPa to 3.7MPa. Depressurization subsequently continued by opening the valve from t = 650min to t = 830min until reaching atmospheric pressure. The temperature was continuously monitored during controlled depressurization by a thermocouple located 422mm from the valve.

A 2-D axisymmetric finite element model consisting of 750 elements was adopted to represent the cylindrical sample. The initial conditions are comparable with those reported by Yun et al. (2011), namely: P =12MPa, T = 3.5°C, S_h = 0.195, ϕ = 0.75, and an intrinsic (isotropic) permeability with k_0 = $0.5 \times 10^{-13} m^2$. An impermeable flow boundary around the shell was assumed except at the ball-valve position, where the depressurization rates discussed above were imposed. Furthermore, we adopted Equation (29) for the thermal conductivity with β' = -0.2; Equation (13) for the capillary pressure with parameters P_0 = 0.1MPa, m_{bc} = 1.2, C_1 = 3, and C_2 = 2. The methane hydrate phase boundary (Equation 3) was assumed with a salt concentration = 2.05wt%. As for the mechanical model (Equation 31), the following parameters were used: E_{Hyd} = 1.35GPa, E_{Sed} = 0.03GPa (Waite et al., 2009), b = 0, c = 1, and d = 1. We considered the relative permeability for liquid and gas phase by adopting Equation (T2.3) with a = 3 and b = 3.

Figure 11a shows the evolution of the experimental and simulated *P-T* trajectories. The endothermic behavior of hydrate dissociation is captured by the model and shows a sharp change of the *P-T* path trajectory upon meeting the methane hydrate phase boundary. The heat consumed during hydrate dissociation induces a significant cooling of the sample and brings the *P-T* trajectory to the ice/liquid-

water boundary. Once hydrate dissociation is complete, the path leaves the phase boundary and temperature increases due to both ambient heat and the exothermic character of ice formation. Figure 11b presents the experimental and simulated pressure evolution. The model captures the experimental depressurization rates mentioned above, as well as the slight pressure rebound between t = 180min to t = 650min (induced by the closed valve condition). Figure 11c compares experimental and modelled gas productions and shows the pseudo-kinetic model to accurately simulate the maximum amount of produced gas. The evolution of temperature during the experiment is also accurately simulated (Figure 11d).

5.4. Modeling gas hydrate and ice formation in permafrost settings

After applying the proposed approach to solve short-term rates of gas hydrate dissociation, we here present a long-term 1-D simulation that involves a complex *P-T* trajectory associated with the formation of gas-methane hydrate and ice in permafrost settings. The 1-D analysis is based on published data from the Mount Ebert site, on the Alaska North Slope, which is briefly summarized below.

Dai et al. (2011) reconstructed the evolution of ground surface elevation (GSE), ground surface temperature (GST), the gas hydrate stability zone (GHSZ), and the base of ice bearing permafrost (BIPF) at the Mount Elbert site (Figure 12). The study was based on available data on surface and subsurface temperatures, and stratigraphy and geology from well logs and regional data (see Dai et al., 2011). It was assumed that continuous permafrost formed when the mean annual ground surface temperature was below -5°C and the temperature at the BIPF was -1°C. A linear geothermal gradient of 1.64°C/100m and 3.56°C/100m are considered above the BIPF and below the permafrost, respectively (Lachenbruch et al., 1982; Collett et al., 1988; Collet, 1993). The fluid pressure is hydrostatic and the water table was assumed to be at GSE. Two main formations with high S_h (i.e. 60-75%) were identified in this area: Unit D (depth ~ 614-628m), and a deeper Unit C (depth ~ 650-666m) (Moridis et al., 2011).

Our simulation is based on the conditions in Unit C (Figure 13). We adopt an intrinsic (isotropic) sediment permeability of $k_0 = 1.0 \times 10^{-12} m^2$ (at $\phi_0 = 0.35$) (Anderson et al, 2011); Equation (29) for the thermal conductivity with β' = -0.2; Equation (10) for the capillary pressure with parameters P_0 = 0.1MPa, m = 0.5, and Equation (9) for establishing the rate of ice transition with q_i = 0.99. The hydrostatic pressure is calculated based on the GSE; and the temperature evolution at this level is estimated based on both the BIPF/GST and the corresponding geothermal gradients from Dai et al. (2011). According to Winters et al. (2011), the presence of highly permeable sediments within the gas hydrate stability zone is essential for the formation of GHBS. Two possible scenarios were proposed to explain the presence of gas hydrate in these layers (Dai et al., 2011): i) pre-existing gas reservoirs were transformed into GHBS by favorable *P-T* conditions; ii) gas hydrate formed from biogenic gas or thermogenic gas that migrated

into the stability zone from deeper strata. We adopt the second scenario and assume that the sediment is almost fully saturated (S^*_l = 0.997), with a small amount of methane in the pore space (S^*_g = 0.003), maintained constant by controlling the capillary pressure in the modeling. The sediment is initially in Zone A, with P_i= 6.1MPa; T_i = 22.43°C; S_{hf} = S_{if} = 0.0. The *P-T* changes depicted in Figure 13a are imposed and hydrate starts to form when the *P-T* path meets the phase boundary as a result of a rise in GSE and a reduction in GST. Hydrate formation continues under excess water conditions with a progressive reduction of S_l (i.e. because the volume of voids is gradually occupied by hydrate). Under the assumed conditions, the model predicts a final S_h ~ 0.63, which is compatible with reported values (Hunter et al., 2011; Kneafsey et al., 2011; Lee & Collet, 2011; Moridis et al., 2011). No ice forms under the conditions assumed for this unit.

We also simulate conditions associated with ice formation within a shallower layer at 300m depth, within which no gas hydrate was reported. The assumed pressure and temperature evolutions (Figure 14a) are based on both the hydrostatic pressure from the GSE, and the geothermal gradients based on the GST (as discussed above). In line with scenario i) discussed above (Dai et al., 2011), we consider pre-existing methane gas and liquid water, S_{li} = 0.7; S_{gi} = 0.3. The analysis starts in stability Zone A (Figure 14b), with hydrate and ice not present. These assumptions are compatible with Figure 12 and show that at the beginning of the analysis (i.e. ~ $2x10^6$ years ago), prevailing conditions were neither located inside the GHSZ nor above the BIPF. The subsequent rise in GSE and reduction in GST provide favorable conditions for hydrate formation. When the *P-T* path meets the methane hydrate phase boundary (i.e. Zones A to B, point 1, Figure 14b), hydrate forms by consuming the available methane and water. Since the volume of methane hydrate formed is less than the total consumption of methane and water volumes, liquid saturation increases as water from upper layers occupies the difference in volume. It is assumed that the migration of methane gas from lower layers is prevented due to low permeability strata. Subsequent GST reductions cause the formation of permafrost (i.e. the *P-T* path from Zones B to D, point 2, Figure 14b) and expand the zone of methane hydrate stability by cooling deeper sediments. Although there are subsequent fluctuations in the *P-T* path (because of variations in GST), the sediment remains in Zone D, therefore no phase changes occur. Under these conditions, the model predicts the formation of ice (S_{if} ~ 0.94) and only small amount of hydrate (S_{hf} ~ 0.06).

The simple cases presented above do not exactly replicate the Mount Elbert conditions, but confirm that the pseudo-kinetic phase-change model is able to simulate, in a general manner, some of the scenarios proposed to explain the presence of gas hydrate and ice in the different layers at this site.

6. Discussion

The kinetic model of Kim et al. (1987) and the pseudo-kinetic model, proposed in this work are both empirical models, because most of the parameters are calibrated/determined from laboratory tests. For example, the kinetic constant (k_d Equation 6) requires empirical determination of the parameter k_{do}. Moreover, this parameter is not directly obtained from tests, but is calibrated from gas hydrate dissociation experiments. The activation energy (ΔE_a, Equation 6) is also obtained from experiments. The Kim et al. (1987) kinetic model further requires estimation of the gas hydrate reaction surface area (A_s, Equation 5), defined as the interface area between hydrate and surrounding phases, and requires simplified assumptions to estimate the gas hydrate particle size and the related reaction surface area. As discussed in Sun & Mohanty (2006), estimation of the surface area remains contentious, and various equations (some with additional constants that need to be determined) have been suggested for this parameter (e.g. Yousif et al., 1991; Masuda et al., 2002; Moridis et al., 2005). There is no consensus on which of these equations is the most appropriate for analyses involving GHBS. Most of the parameters discussed above have a physical meaning.

Our proposed pseudo-kinetic model has the advantage that only one constant (i.e. q_{hd}, Equation 7) needs to be determined from experiments, as opposed to the three (plus) parameters required by the kinetic model of Kim et al. (1987). Furthermore, the pseudo-kinetic model constant has a physical meaning, i.e. it controls the rate of gas hydrate dissociation. The pseudo-kinetic model works on the *P-T* plane, the space generally adopted to analyze problems involving gas hydrate formation and dissociation, and is easy to implement in numerical codes. It is worth noting that GHBS numerical codes are generally formulated in terms of pressure (or saturation) and temperature. Whereas the kinetic model of Kim et al. (1987) is based on fugacity and temperature and so requires additional calculations to transform pressure to fugacity. In contrast, the proposed pseudo-kinetic model is directly expressed in terms of pressure and temperature, with associated saving in computational time.

To capture better the experimentally observed dependence of gas hydrate dissociation rate on hydrate saturation (particularly at low S_h), we proposed a slight modification of the pseudo-kinetic model to include a dependence on S_h (Equation 32, Section 5.1). Interestingly, to improve on the kinetic law proposed by Kim et al. (1987), subsequent models have also incorporated S_h in their formulations (e.g. Yousif et al., 1991; Masuda et al., 2002; Moridis et al., 2005; Sun & Mohanty, 2006), particularly when calculating A_s.

The kinetic model of Kim et al. (1987) was based on experimental results from gas hydrate dissociation under different thermodynamic conditions. The proposed pseudo-kinetic model, implemented in a full coupled THCM finite element code, was validated against these same experimental results and then

further evaluated against a variety of synthetic cases. The synthetic cases covered several *P-T* trajectories and demonstrated the ability of the pseudo-kinetic model to deal with phase transformations under a range of different conditions involving GHBS. In addition, simulations of results from natural gas hydrate, both over the short-term (14hours, scale methane production test of a GHBS core offshore Korea) and long-term ($2x10^6$ years, modeling of methane hydrate and ice formation in a permafrost setting in Alaska), demonstrate the ability of the pseudo-kinetic approach to reproduce phase transformations in problems involving very different time scales, in which either kinetic or equilibrium conditions are dominant.

We propose specific functions (Equations 7, 9, and 32) to model phase changes in GHBS, which may be modified in future as necessary. However, the main idea advanced in this work is to express the rate of phase transformation as a function of the distance between the current state and the phase boundary. We have shown that this concept can be used to satisfactorily model both gas hydrate formation/dissociation and ice formation/thawing, illustrating the consistency of the proposed pseudo-kinetic approach. We have evaluated the model by solving problems mainly involving pressure and temperature perturbations. Further studies should be conducted to investigate other effects in GHBS phase transformations, such as geo-chemical interactions.

7. Conclusions

Based on previously published experimental evidence, we propose a new model for gas hydrate dissociation that relates the rate of gas hydrate dissociation to the distance between the current state and the phase boundary in *P-T* space. The model incorporates only one parameter that is easily calibrated from laboratory tests and controls the rate of gas hydrate dissociation. This is a clear advantage with respect to the kinetic model that is currently used to simulate gas hydrate dissociation, which requires the determination of multiple parameters and constants (generally 3+). The proposed approach can be used to simulate gas hydrate formation/dissociation, as well as ice formation/thawing. As the structure of the model is simple and is formulated in the *P-T* space, its implementation in numerical simulators for GHBS is relatively easy and cost-effective.

The proposed pseudo-kinetic model was implemented in a fully coupled THCM finite element code and applied to simulate different problems involving GHBS, including synthetic cases as well as data available on the behavior of marine gas hydrate over short timescales, and permafrost gas hydrate over long timescales. The performance of the pseudo-kinetic model in all cases was satisfactory and demonstrates its applicability to a wide range of *P-T* trajectories. We argue that the pseudo-kinetic model provides a simple and powerful alternative to the kinetic model to simulate phase changes in GHBS. Future studies should investigate how the model handles the effect of chemical interactions (e.g. water salinity) on rates of methane hydrate dissociation.

Acknowledgements:

We acknowledge the financial support from NETL (National Energy Technology Laboratory), DOE, USA, through Award No.: DE-FE0013889.

633 *References*

634 Ahmadi, G., Ji, C., & Smith, D. H. 2004. Numerical solution for natural gas production from methane
635 hydrate dissociation. *Journal of petroleum science and engineering*, 41(4): 269-285.

636 Anderson, B.J., Kurihara, M., White, M.D., Moridis, G.J., Wilson, S.J., Pooladi-Darvish, M., Gaddipati,
637 M., Masuda, Y., Collet, T.S., Hunter, R.B., Narita, H., Rose, K., & Boswell, R., 2011. Regional long-term
638 production modeling from a single well test, Mount Elbert Gas Hydrate Stratigraphic Test Well, Alaska
639 North Slope. *Marine and Petroleum Geology*, 28: 493-501.

640 Boswell, R., 2009. Is gas hydrate energy within reach? *Science*, 325: 957–958.

641 Brooks, R.H., & Corey, A.T., 1964. Hydraulic properties of porous media. *Hydrology Papers*, Colorado
642 State University, Fort Collins 3, 24.

643 Chen, L., Yamada, H., Kanda, Y., Okajima, J., Komiya, A., & Maruyama, S., 2017. Investigation on the
644 dissociation flow of methane hydrate cores: numerical modelling and experimental verification. *Chemical*
645 *Engineering Science*, 163: 31-43.

646 Cheng, Y., Li, L., Yuan, Z., Wu, L., & Mahmood, S., 2013. Finite element simulation for fluid solid
647 coupling effects on depressurization induced gas production from gas hydrates reservoirs. *Journal of*
648 *Natural Gas Science and Engineering*, 10, 1-7.

649 Clarke, M., & Bishnoi, P.R., 2000. Determination of the intrinsic rate constant of ethane gas hydrate
650 decomposition. *Chemical Engineering Science*, 55: 4869-4883.

651 Clarke, M., & Bishnoi, P.R., 2001. Determination of the activation energy and intrinsic rate constant of
652 methane gas hydrate decomposition. *The Canadian Journal of Chemical Engineering*, 79: 143-147.

653 Civan, F., 2000. Predictability of porosity and permeability alterations by geochemical and
654 geomechanical rock and fluid interactions. *SPE* 58764.

655 Clement, T.P., Hooker, B.S., & Skeen, R.S., 1996. Macroscopic models for predicting changes in
656 saturated porous media properties caused by microbial growth. *Ground Water* 34: 934-942.

657 CODE_BRIGHT Manual, 2018. *https://deca.upc.edu/en/projects/code_bright/downloads*, accessed on
658 Oct. 11th, 2019.

659 Collett, T.S., 1993. Natural gas hydrate of Prudhoe Bay and Kuparuk River area, North Slope, Alaska.
660 *AAPG Bulletin*, 77 (5): 793e812.

661 Collett, T.S., Bahk, J.J., Baker, R., Boswell, R., Divins, D., Frye, M., Goldberg, D., HusebΘ, J., Koh, C.,
662 Malone, M., Morell, M., Myers, G., Shipp, C., & Torres, M., 2015. Methane hydrate in nature – Current
663 knowledge and challenges. *Journal of Chemical Engineering Data*, 60: 319-329.

664 Collett, T.S., Bird, K.J., Kvenvolden, K.A., & Magoon, L.B., 1988. Geologic interrelations relative to gas
665 hydrates within the North Slope of Alaska. *USGS* Open-File Report 88-389.

666 Collett, T.S., Lee, M.W., Agena, W.F., Miller, J.J., Lewis, K.A., Zyrianova, M.V., Boswell, R., & Inks,
667 T.L., 2011. Permafrost-associated natural gas hydrate occurrences on the Alaska North Slope. *Marine*
668 *and Petroleum Geology,* 28: 279-294.

669 Dai, S., Lee, Ch., & Santamarina, J.C., 2011. Formation history and physical properties of sediments from
670 the Mount Elbert Gas Hydrate Stratigraphic Test Well, Alaska North Slope. *Marine and Petroleum*
671 *Geology* 28: 427-438.

672 De La Fuente, M., Vaunat, J., & Marín-Moreno, H., 2019. Thermo-Hydro-Mechanical Coupled Modeling
673 of Methane Hydrate-Bearing Sediments: Formulation and Application. Energies, 12, 2178.

674 Englezos, P., 1993. Clathrate hydrates. *Ind. Eng. Chem. Res.,* 32: 1251-1274.

675 Englezos, P., Kalogerakis, N., Dholabhai, P.D., & Bishnoi, P.R., 1987a. Kinetics of formation of methane
676 and ethane gas hydrate. *Chemical Engineering Science,* 42: 2647-2658.

677 Englezos, P., Kalogerakis, N., Dholabhai, P.D., & Bishnoi, P.R., 1987b. Kinetics of gas hydrate formation
678 from mixtures of methane and ethane. *Chemical Engineering Science,* 42: 2659-2666.

679 Fang, H.L., 2009. A fully coupled thermo-hydro-mechanical model for methane hydrate reservoir
680 simulations. *Int. Symp. On Geoenvironmental Eng*. ISGE2009.

681 Gai, X., & Sánchez, M. 2017. A Geomechanical model for gas hydrate bearing sediments. *Environmental*
682 *Geotechnics*, 4(2): 143–156.

683 Gamwo, I.K., & Liu, Y., 2010. Mathematical modeling and numerical simulation of methane production
684 in a hydrate reservoir. *Ind. Eng. Chem. Res.,* 49: 5231-5245.

685 Gupta, S., Helmig, R., & Wohlmuth, B., 2015. Non-isothermal, multi-phase, multi-component flows
686 through deformable methane hydrate reservoirs. *Comput Geosci*, I19:1063-1088.

687 Haligva, C., Linga, P., Ripmeester, J.A., & Englezos, P., 2010. Recovery of methane from a variable
688 volume bed of silica sand/hydrate by depressurization. *Energy Fuels,* 24: 2947-2955.

689 Hunter, R.B., Collett, T.S., Boswell, R., Anderson, B.J., Digert, S.A., Pospisil, G., Baker, R., & Weeks,
690 M., 2011. Mount Elbert gas hydrate stratigraphic test well, Alaska North Slope: Overview of scientific
691 and technical program. *Marine and Petroleum Geology,* 28: 295-310.

692 Jamaludin, A.K., Kalogerakis, N., & Bishnoi, P.R., 1989. Modeling of decomposition of a synthetic core
693 of methane gas hydrate by coupling intrinsic kinetics with heat transfer rates. *Canadian Journal of*
694 *Chemical Engineering,* 67: 948-954.

695 Kamath, V., & Godbole, S., 1987. Evaluation of hot-brine stimulation technique for gas production from
696 natural gas hydrates. *Journal of petroleum technology,* 39(11): 1379-1388.

697 Kim, H.C., Bishnoi, P.R., Heidemann, R.A., & Rizvi, S.S.H. 1987. Kinetics of methane hydrate
698 decomposition. *Chemical Engineering Science,* 42: 1645-1653.

699 Kimoto, S., Oka, F., & Fushita, T., 2010. A chemo-thermo-mechanically coupled analysis of ground
700 deformation induced by gas hydrate dissociation. *International Journal of Mechanical Sciences*, 52(2):
701 365-376.

702 Kimoto, S., Oka, F., Fushita, T., & Fujiwaki, M. 2007. A chemo-thermo-mechanically coupled numerical
703 simulation of the subsurface ground deformations due to methane hydrate dissociation. *Computers and*
704 *Geotechnics*, 34(4): 216-228.

705 Klar A, Soga K, & Ng M. 2010. Coupled deformation–flow analysis for methane hydrate extraction.
706 *Geotechnique,* 60(10): 765–76.

707 Kneafsey, T.J., Lu, H., Winters, W., Boswell, R., Hunter, R., & Collett, T.S., 2011. Examination of core
708 samples from the Mount Elbert gas hydrate stratigraphic test well, Alaska North Slope: effects of retrieval
709 and preservation. *Marine and Petroleum Geology,* 28: 381-393.

710 Kneafsey, T.J., Tomusta, L., & Moridis, G.J., 2005. Methane hydrate formation and dissociation in a
711 partially saturated sand – Measurements and observations. *Lawrence Berkeley National Laboratory*.

712 Kneafsey, T.J., Tomusta, L., Moridis, G.J., Seol, Y., Freifeld, B.M., Taylor, C.E., & Gupta, A., 2007.
713 Methane hydrate formation and dissociation in a partially saturated sand sample. *Journal of Petroleum*
714 *Science and Engineering,* 56: 108-126.

715 Kowalsky, M.B., & Moridis, G.J., 2007. Comparison of kinetic and equilibrium reaction models in
716 simulating gas hydrate behavior in porous media. *Energy Conversion & Management*, 48: 1850-1863.

717 Kwon, T. H., Cho, G. C., & Santamarina, J. C., 2008. Gas hydrate dissociation in sediments: Pressure-
718 temperature evolution. *Geochem. Geophys. Geosyst*, 9(3): Q03019.

719 Lachenbruch, A.H., Sass, J.H., Marshall, B.V., & Moses Jr., T.H., 1982. Permafrost, heat flow, and the
720 geothermal regime at Prudhoe Bay, Alaska. *Journal of Geophysical Research* 87, (B11): 9301-9316.

721 Lee, M.W., & Collett, T.S., 2011. In-situ gas hydrate hydrate saturation estimated from various well logs
722 at the Mount Elbert Gas Hydrate Stratigraphic Test Well, Alaska North Slope. *Journal of Marine and*
723 *Petroleum Geology*, 28: 439-449.

724 Liang, H., Song, Y., &Chen, Y., 2010. Numerical simulation for laboratory scale methane hydrate
725 dissociation by depressurization. *Energy Conservation and Management*, 51: 1883-1890.

726 Makogon, Y.F., 2010. Natural gas hydrates – A promising source of energy. *Journal of Natural Gas*
727 *Science and Engineering*, 2: 49–59.

728 Makogon, Y.F., Holditch, S.A., & Makogon, T.Y., 2007. Natural gas-hydrate – A potential energy source
729 for the 21st Century. *Journal of Petroleum Science and Engineering*, 56: 14–31.

730 Masuda, Y., Kurihara, M., Ochuchi, H., & Sato, T., 2002. A filed-scale simulation study on gas
731 productivity of formations containing gas hydrates. *Proceedings of the Fourth International*
732 *Conference on Gas Hydrates*, Yokohama, Japan.

733 Milkov, A.V., & Sassen, R., 2002. Economic geology of offshore gas hydrate accumulations and
734 provinces. *Marine and Petroleum Geology*, 19:1-11.

735 Minagawa, H., Nishikawa, Y., Ikeda, I., Sakamoto, Y., Miyazaki, K., Takahara, N., Komai, T., & Narita,
736 H., 2008. Relation between permeability and pore-size distribution of methane-hydrate-bearing
737 sediments. *Proceedings from the Offshore Technology Conference*, Houston, Texas; USA.

738 Moridis, G.J., 2014. TOUGH+HYDRATE v1.2 User's Manual: A code for the simulation of system
739 behavior in hydrate bearing geologic media. *LBNL-0149E-Rev*

740 Moridis, G.J., Seol, Y., & Kneafsey, T.J., 2005. Studies of reaction kinetics of methane hydrate
741 dissociation in porous media. *Lawrence Berkeley National Laboratory*.

742 Moridis, G.J., Silpngarmlert, S., Reagan, M.T., Collet, T., & Zhang, K., 2011. Gas production from a
743 cold, stratigraphically-bounded gas hydrate deposit at the Mount Elbert gas hydrate stratigraphic test well,
744 Alaska North Slope: Implications of uncertainties. *Marine and Petroleum Geology*, 28: 517-534.

745 Nazridoust, K., & Ahmadi, G., 2007. Computational modeling of methane hydrate dissociation in a
746 sandstone core. *Chemical engineering science*, 62(22): 6155-6177.

747 Olivella, S., Gens, A., Carrera, J., & Alonso, E.E., 1996. Numerical formulation for a simulator (CODE-
748 BRIGHT) for the coupled analysis of saline media. *Engineering Computations*, 13/7:87-112.

749 Olivella, S., Carrera J., Gens, A., & Alonso, E.E., 1994. Non-isothermal multiphase flow of brine and gas
750 through saline media. *Transport in porous media*, 15: 271-293.

751 Pooladi-Darvish, M., 2004. Gas production from hydrate reservoirs and its modeling. *Journal of*
752 *Petroleum Engieenrs* SPE-86827-JPT.

753 Rempel, A., & Buffett, B., 1997. Formation and accumulation of gas hydrate in porous media. *Journal of*
754 *Feophysical GEOPHYSICAL RESEARCH-ALL SERIES*-, 102: 10-10.

755 Rempel, A., & Buffett, B., 1998. Mathematical models of gas hydrate accumulation. *Geological Society*,
756 137: 63-74.

757 Rockhold, M.L., Yarwood, R.R., Niemet, M.R., Bottomley, P.J., & Selker, J.S., 2002. Consideration for
758 modelling bacterial-induced changes in hydraulic properties of variably saturated porous media. *Adv.*
759 *Water Resource*, 25: 477-495.

760 Ruan, X., Song, Y., Liang, H., Yang, M., & Dou, B., 2012. Numerical simulation of the gas production
761 behavior of hydrate dissociation by depressurization in hydrate bearing porous medium. *Energy & Fuels*,
762 26: 1681-1694.

763 Rutqvist, J., & Moridis, G.J., 2007. Numerical studies of geomechanical stability of hydrate bearing
764 sediments. *Offshore Technological Conference, Houston, USA*, OTC 18860.

765 Sánchez, M., Gai, X., & Santamarina, J. C. 2017. A constitutive mechanical model for gas hydrate
766 bearing sediments incorporating inelastic mechanisms. *Computers and Geotechnics*, 84: 28–46.

767 Sánchez, M., & Santamarina, J.C., (2016). THCM coupled model for hydrate-bearing sediments: data
768 analysis and design of new field experiments (marine and permafrost settings). *Final Scientific/Technical*
769 *Report Project DE-FE0013889*. United States Department of Energy National Energy Technology.

770 Sánchez, M., Santamarina, C., Teymouri, M., & Gai, X., 2018. Coupled numerical modeling of gas
771 hydrate bearing sediments form laboratory to field scale analyses. *Journal of Geophysical Research: Solid*
772 *Earth*. https://doi.org/10.1029/2018JB015966.

773 Santamarina, J.C., & Ruppel, C., 2008. The impact of hydrate saturation on the mechanical, electrical,
774 and thermal properties of hydrate-bearing sand, silts, and clay. *Proceedings of the 6th International*
775 *Conference on Gas Hydrates*, Vancouver, B.C. Canada, July 6–10, CD-ROM.

776 Santamarina, J.C., & Ruppel, C., 2010. The impact of hydrate saturation on the mechanical, electrical and
777 thermal properties of hydrate-bearing sands, silts and clay, in geophysical characterization of gas
778 hydrates. *SEG Geophysical Developments Series*, No. 14, Editors M. Riedel, E.C. Willoughby, and S.
779 Chopra, pp. 373-384.

780 Sloan, E.D., 1998. Gas Hydrates: Review of Physical/Chemical Properties. *Energy & Fuels*, 12: 191-196.

781 Sloan, E.D., 2003. Fundamental principles and applications of natural gas hydrates. *Nature* 426: 353-363.

782 Sloan, E.D., & Koh, C.A., 2008. Clathrate hydrates of natural gases. *CRC*.

783 Soga, K., Lee, S.L., Ng, M.Y.A., & Klar, A., 2006. Characterisation and engineering properties of
784 methane hydrate soils. *Characterisation and engineering properties of natural soils*, 4: 2591-2642.

785 Sun, J., Ning, F., Lei, H., Gai, X., Sánchez, M., Lu, J., Li, Y., Liu, L., Liu, Ch., Wu, N., He, Y., & Wu,
786 M., 2018. Wellbore stability analysis during drilling through marine gas hydrate-bearing sediments in
787 Shenhu area: A case study. *Journal of Petroleum Science and Engineering*, 170: 345–367.
788 https://doi.org/10.1016/j.petrol.2018.06.032

789 Sun, X., Mohanty, & K.K., 2006. Kinetic simulation of methane hydrate formation and dissociation in
790 porous media. *Chemical Engineering Science*, 61: 3476-3495.

791 Taber, S., 1929. Frost heaving. *The Journal of Geology*, 37(5): 428–461. https://doi.org/10.1086/623637

792 Uchida, S., Soga, K., & Yamamoto, K. 2012. Critical state soil constitutive model for methane hydrate
793 soil. *Journal of Geophysical Research,*117: B03209.

794 van Genuchten, R., 1978. Calculating the unsaturated hydraulic permeability conductivity with a new
795 closed-form analytical model. *Water Resource Research*, 37(11): 21-28.

796 Wagner, W., & Kretzschmar, H.J., 2008. International Steam Tables, 2nd edition. *Springer Verlag*, Berlin,
797 Heidelberg, 2008.

798 Waite, W.F., Santamarina, J.C., Cortes, D.D., Dugan, B., Espinoza, D.N., Germaine, J., Jang, J., Jung,
799 J.W., Kneafsey, T.J., Shin, H., Soga, K., Winters, W.J., & Yun, T.S., 2009. Physical properties of
800 hydrate-bearing sediments. Reviews of Geophysics, 47, RG4003. https://doi.org/10.1029/2008RG000279
801 *American Geophysical Union*, 8755-1209/09/2008RG000279.

802 Winters, W., Walker, M., Hunter, R., Collet, T., Boswell, R., Rose, K., Waite, W., Torres, M., Patil, S., &
803 Dandekar, A., 2011. Physical properties of sediment from the Mount Elbert gas hydrate stratigraphic test
804 well, Alaska North Slope. *Marine and Petroleum Geology,* 28: 361-380.

805 Yin, Z., Chong, Z.R., Tan, H.K., & Linga, P., 2016. Review of gas hydrate dissociation kinetic models for
806 energy recovery. *Journal of Natural Gas Science and Engineering*, 35: 1362-1387.

807 Yousif, M.H., Abass, H.H., Selim, M.S., & Sloan, E.D., 1991. Experimental and theoretical investigation
808 of methane-gas-hydrate dissociation in porous media. *SPE Reservoir Engineering,* 6: 69-76.

809 Younglove, B., & Ely, J., 1987. Thermophysical properties of fluids. II. Methane, ethane, propane,
810 isobutane, and normal butane. *Journal of physical and chemical reference data*, 16: 577-798.

811 Yun, T.S., Fratta, D., & Santamarina, J.C., 2010. Hydrate-Bearing Sediments from the Krishna− Godavari
812 Basin: Physical Characterization, Pressure Core Testing, and Scaled Production Monitoring. *Energy &*
813 *Fuels*, 24: 5972-5983.

814 Yun, T.S., Lee, C., Lee, J.S., Bahk, J.J., & Santamarina, J.C., 2011. A pressure core based
815 characterization of hydrate bearing sediments in the Ulleung Basin, Sea of Japan (East Sea). *Journal of*
816 *Geophysical Research*, 116, B02204.

Table 1. Specific Energy and Thermal Transport – Selected Representative Values*

Species and Phases	Specific Energy	
	Expression	specific heat - latent heat
water - vapour	$e_g^w = L_{evap} + c_{wv}\left(T - T_o\right)$	L_{evap}= 2257 J.g^{-1} c_{wv} = 2.1 J.g^{-1}K^{-1}
water - liquid	$e_w = c_{wl}\left(T - T_o\right)$	c_{wl} = 4.2 J.g^{-1}K^{-1}
water – ice	$e_{ice} = L_{fuse} + c_{wice}\left(T - T_o\right)$	L_{fuse} = 334 J.g^{-1} c_{wice} = 2.1 J.g^{-1}K^{-1}
methane gas	$e_m = c_m\left(T - T_o\right)$	c_m= 1.9 J.g^{-1}K^{-1} V=const c_m= 2.5 J.g^{-1}K^{-1} P=const
hydrate (1)	$e_h = L_{diss} + c_h\left(T - T_o\right)$	L_{diss}= 339 J.g^{-1} c_h= 2.1 J.g^{-1}K^{-1}
mineral	$e_s = c_s\left(T - T_o\right)$	c_s= 0.7 J.g^{-1}K-1 quartz c_s= 0.8 J.g^{-1}K^{-1} calcite

*Table from Sanchez & Santamarina (2016).

Source: CRC handbook and other general databases. (1) Waite, http://woodshole.er.usgs.gov/operations/hi_fi/index.html; Handa 1986.

Note: the sign of the latent heat is adopted to capture endothermic-exothermic effects during phase transformation.

Table 2. Constitutive equations used in the THCM model.

Description	*Equation*	
The hydraulic conductivity.	$\mathbf{K}_\beta = \mathbf{k}\frac{k_{r\beta}}{\mu_\beta};\qquad \beta = \ell, g$	(T2.1)
The intrinsic permeability, (Minagawa et al. 2008).	$k = k_0 \frac{\phi^3}{(1-\phi)^2}\frac{(1-\phi_0)^2}{\phi_0^3}(1-S_h-S_i)^N$	(T2.2)
The relative permeability for liquid/ gas phase.	$k_{r\ell} = \left(\frac{S_\ell}{S_\ell+S_g}\right)^a = \left(S_\ell^*\right)^a,\ k_{rg} = \left(1-\frac{S_\ell}{S_\ell+S_g}\right)^b = \left(1-S_\ell^*\right)^b$	(T2.3)
Non-advective flux; the Fick's law.	$i_\beta^j = -\mathbf{D}_\beta^j \nabla\theta_\beta^j;\qquad \beta = \ell, g\ ;\ \ j = m, w$	(T2.4)
The viscosity of the liquid phase, (Olivella, 1994).	$\mu_\ell\,[\text{Pa.s}] = 2.1\cdot 10^{-6}\exp\left(\frac{1808.5\ \text{K}}{T}\right)$	(T2.5)
The viscosity of the gas phase, (Younglove & Ely, 1987).	$\mu_g\,[\text{Pa.s}] = 10.3\cdot 10^{-6}\left[1+0.053\frac{P_g}{\text{MPa}}\left(\frac{280\,\text{K}}{T}\right)^3\right]$	(T2.6)
The mass of dissolved methane per unit volume of liquid phase; the Henry's law.	$\theta_l^m = \frac{P_m}{H}\frac{M_m}{M_w}\rho_l$	(T2.7)
The mass of vapor water per unit volume of gas phase; Psychometric law.	$\theta_g^w = \left(\theta_g^w\right)^0 \exp\left(\frac{P_C M_w}{RT\rho_l}\right)$	(T2.8)

Table 3. Index properties of the 10B-17P core specimen (from Yun et al. 2011)

Properties	***Values***	***Device/Technique***
Specific gravity, G_s	2.57	ASTM D854
Specific surface (S_a, m^2/g)	31	N_2 adsorption
Clay content (%)	12	Less than 2 μm
Liquid limit (w_L, %)	115	ASTM D4318
Plastic limit (w_P, %)	65	ASTM D4318
Plastic index (w_L-w_P)	50	
Soil classification	OH or MH	USCS system

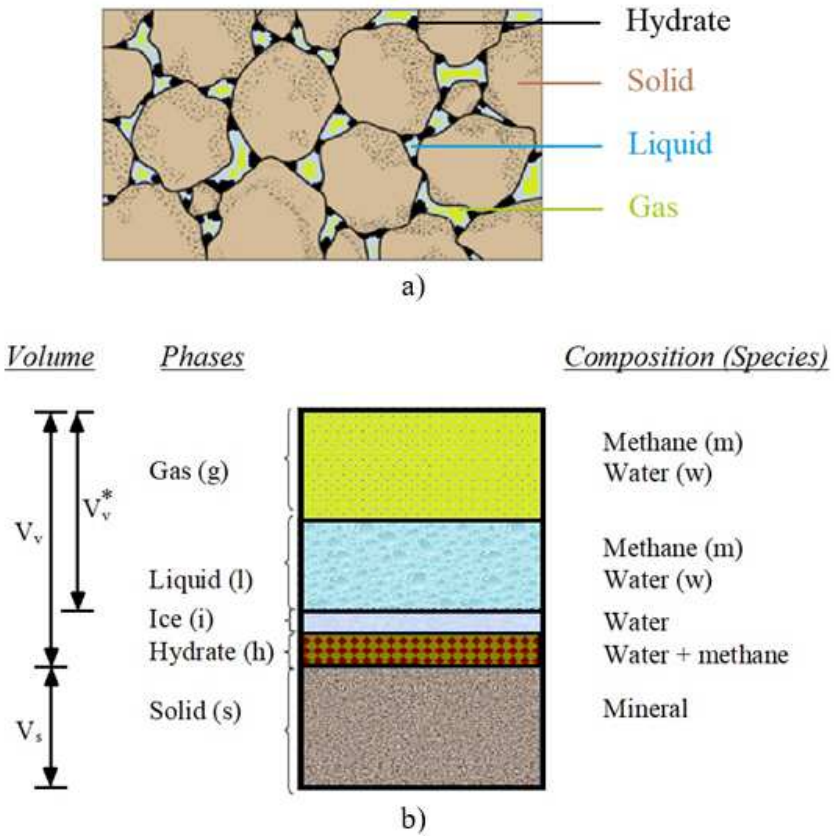

Figure 1. Gas hydrate bearing sediments: a) sketch illustrating the 4 phases typically found in GHBS; and b) schematic representation showing how the 3 species can be encountered in the 5 possible phases considered in this work.

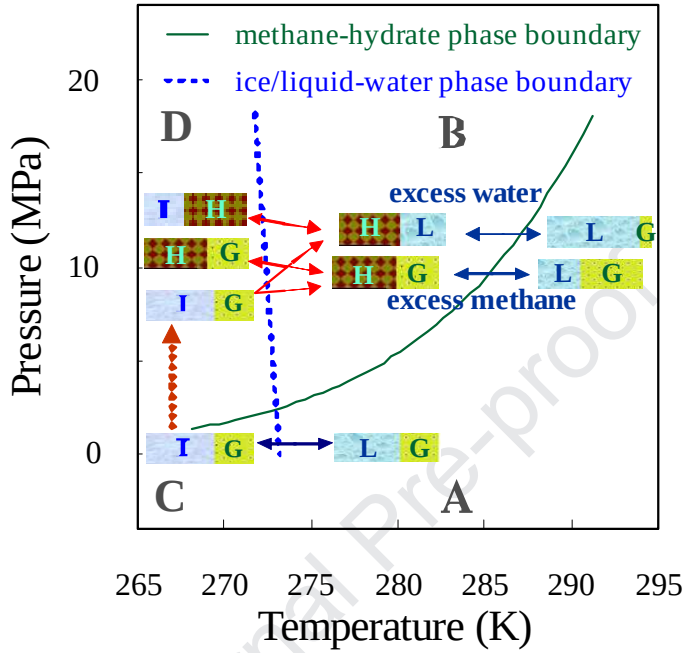

Figure 2. Phase boundaries for water-methane mixtures (based on Eqs. 3 and 4) in the *P*-*T* space showing the four regions (A, B, C, and D, where relevant phases are stable) emerging when the methane-hydrate and ice/liquid-water phase boundaries are superimposed. Ice phase (I) is stable on the left side of ice/liquid-water phase boundary (Zones C and D). Hydrate phase (H) is stable above the methane-hydrate phase boundary (Zones B and D). Hydrate forms upon coexistence of both liquid (L) and gas (G) phases in stable Zone B and it can be either under excess water conditions (i.e., for a given CH_4 mass the H_20 available is ≥ than the required mass to form the hydrate), or under excess methane conditions (i.e. for a given H_20 mass the CH_4 available is > than the required mass to form hydrate). Phases are instable out of their stability zones and engage in phase transformations.

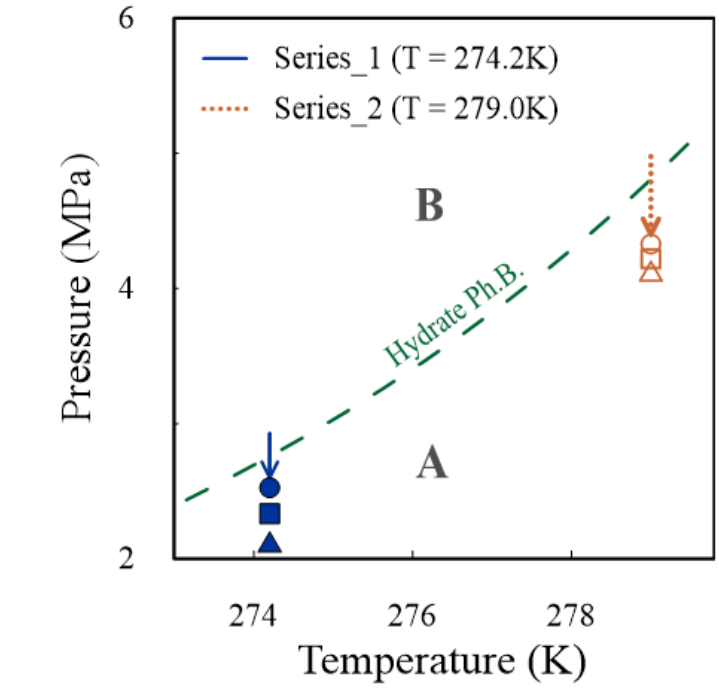

a)

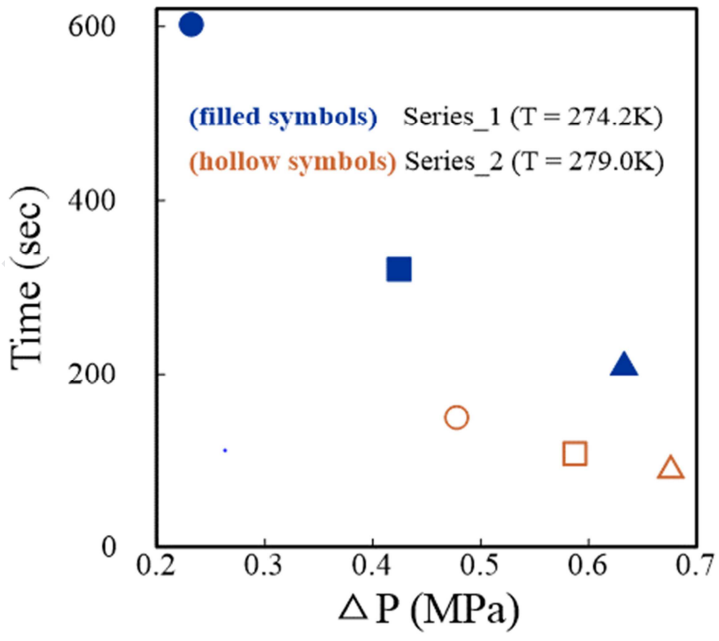

b)

Figure 3. Results from Kim et al. (1987) hydrate dissociation experiments involving depressurization under different pressure gradients (ΔP) at two different constant temperatures: a) *P-T* trajectory moves from stable Zone B to unstable Zone A, leading to hydrate dissociation (each symbol stands for one experiment and shows the induced pressure, Ph.B.: phase

boundary); b) time to achieve complete hydrate dissociation for each experiment for different ΔP values.

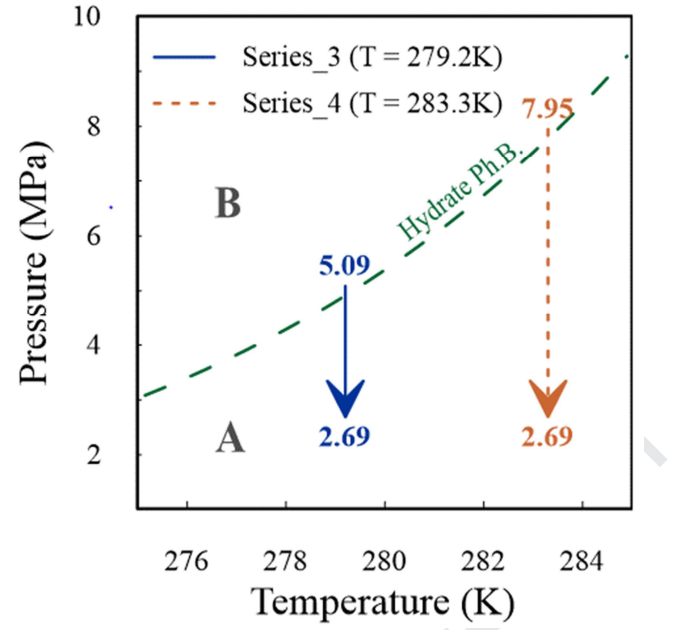

a)

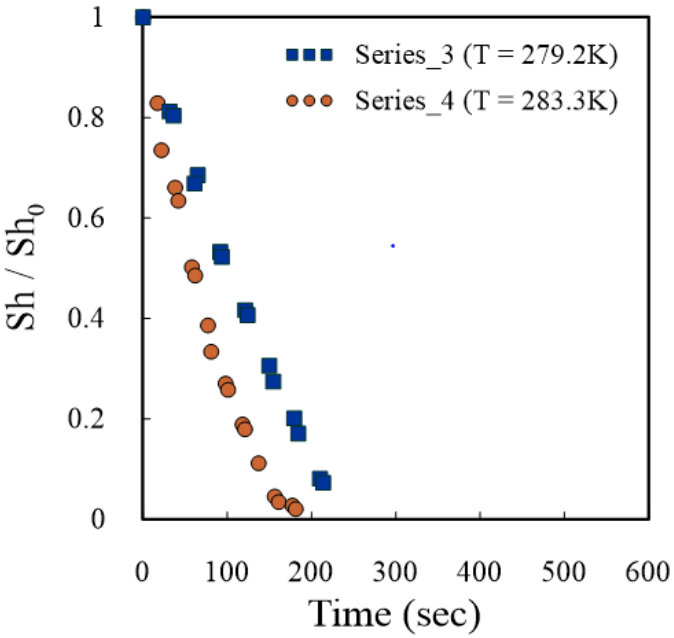

b)

Figure 4. Results from Kim et al. (1987) hydrate dissociation experiments involving depressurization at two different constant temperatures: a) *P-T* paths move from stable Zone B to unstable Zone A leading to hydrate dissociation, b) time evolution of hydrate saturation due to fast depressurizations, the vertical axis shows the ratio of hydrate saturation to its initial value.

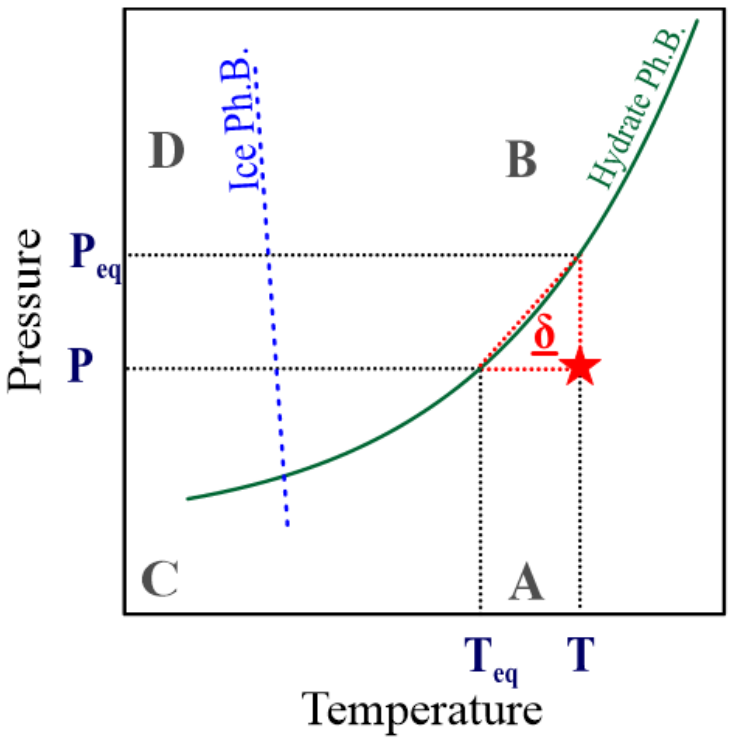

Figure 5. Example of an unstable state in the *P-T* plane with respect to the hydrate phase boundary. The rate of change for an unstable phase (in this case hydrate) is a function of the distance (δ) between the phase boundary (in this case, hydrate phase boundary) and the current *P-T* state (★).

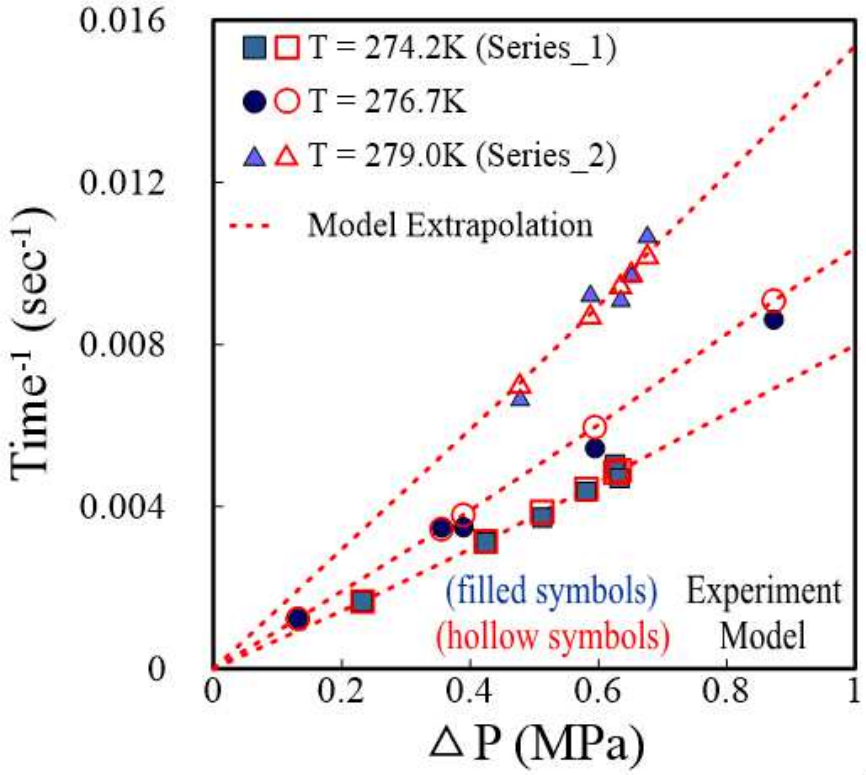

Figure 6. Experimental and pseudo-kinetic model results showing the effect of pressure gradient (ΔP) on the rate of hydrate dissociation at three different constant temperatures. The vertical axis shows the reciprocal of the time at which fully hydrate dissociation was achieved. The dashed lines join the results of tests conducted at the same temperature. The points along the dashed lines correspond to the times at which full hydrate dissociation was achieved under different pressure gradients and at three different temperatures. Experimental data from Kim et al. (1987).

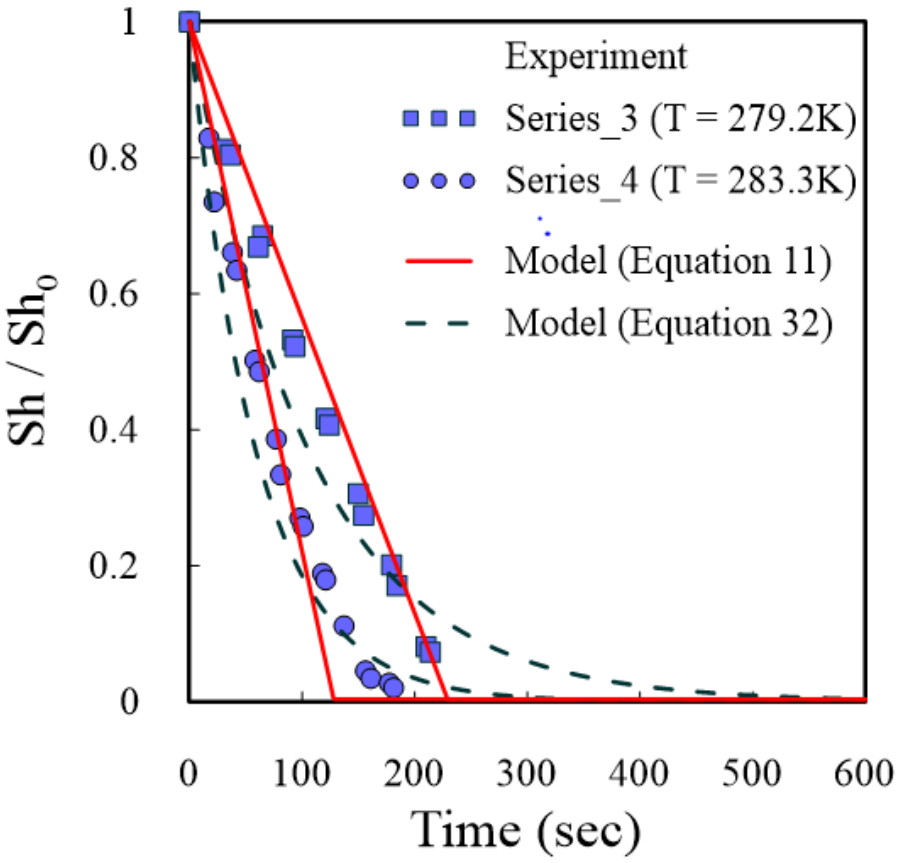

Figure 7. Experimental and pseudo-kinetic model results from hydrate dissociation tests involving depressurization at two different constant temperatures. The solid and dashed lines were obtained after reducing the outputs from numerical simulations based on Eqs. (11) and (32). The vertical axis shows the ratio of hydrate saturation to its initial value. Experimental data from Kim et al. (1987).

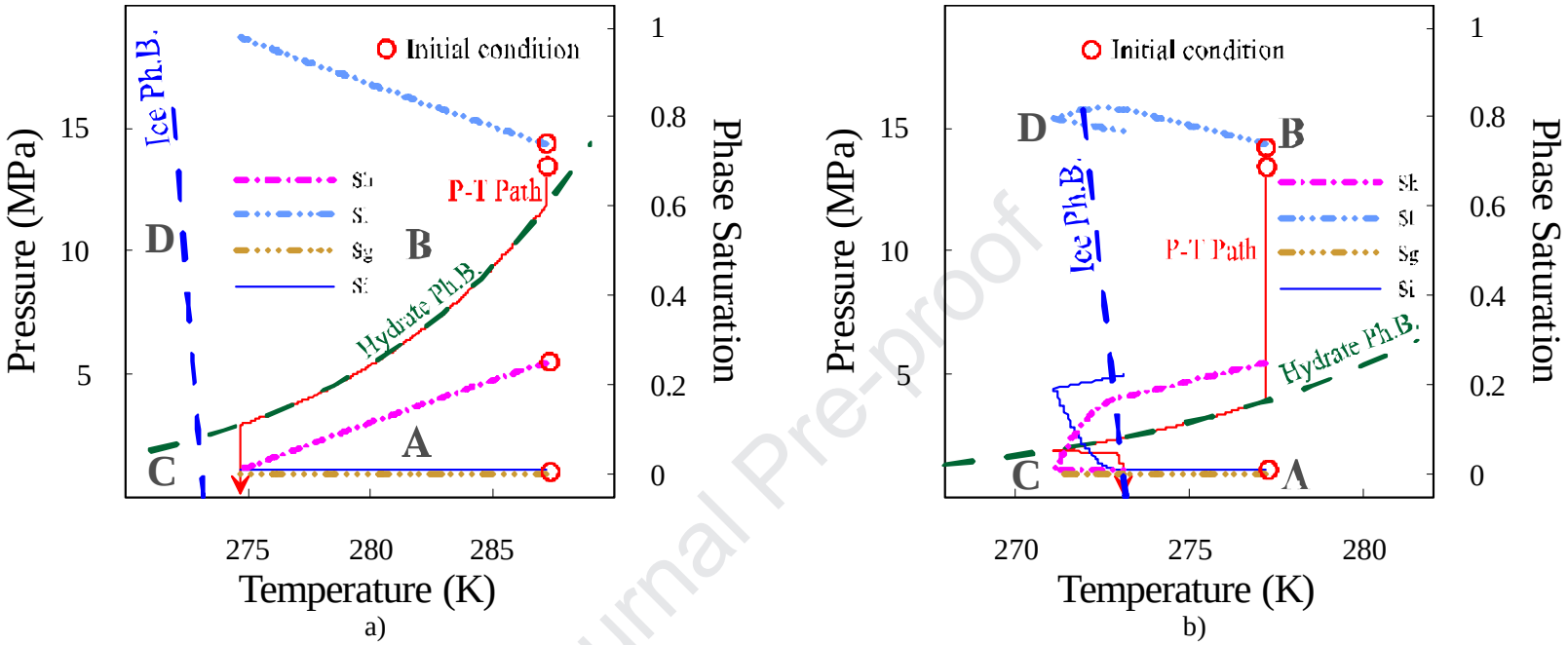

Figure 8. Numerical modeling results showing *P-T* trajectories with the corresponding phase saturation evolutions for two synthetic cases involving hydrate dissociation triggered by depressurization. Both cases start in Zone B with the same initial pressure and phase saturations, but at two different initial temperatures: a) Case I, T_i =287.65K; and b) Case II, T_i =277.15K. In both cases the *P-T* paths move towards the left on reaching the phase boundary (because hydrate dissociation is endothermic) with the corresponding S_h (violet line) decrease and S_l (light-blue line) increase (gas is ejected). In Case II (lower T_i) the *P-T* path crosses the ice/liquid-water phase boundary, with the corresponding increase in S_i (dark-blue line) and the reduction in S_l (light-blue line).

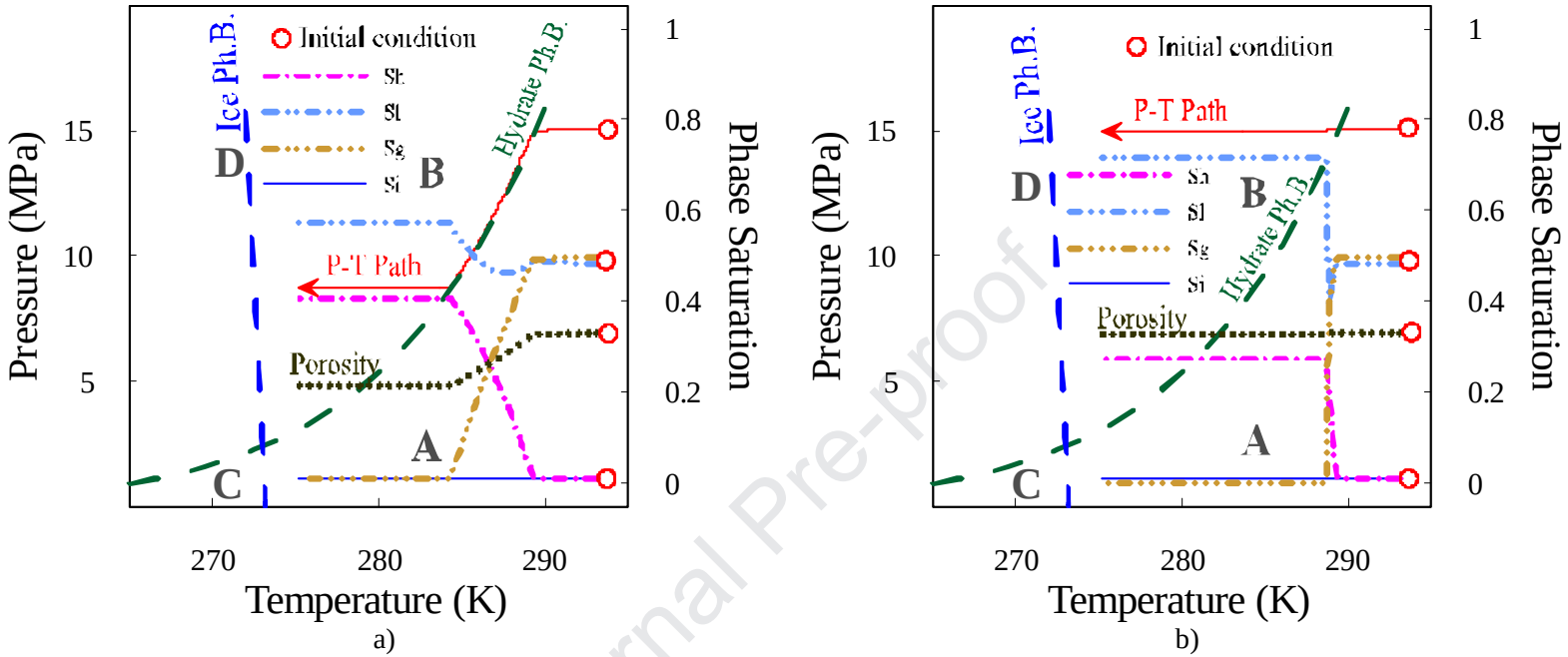

Figure 9. Numerical modeling results showing *P-T* trajectories with the corresponding phase saturation evolutions for two synthetic cases involving hydrate formation by cooling under excess water conditions. Both cases start in Zone A, with the same initial pressure and phase saturations: a) in Case III (i.e., a closed system) the cooling leads to a *P* reduction because the *P-T* path follows the hydrate phase boundary with a progressive hydrate formation (violet line), methane consumption (brown line), and S_l (light blue) increase as gas vanishes; b) in Case IV hydrate forms and methane consumes upon the *P-T* trajectory meeting the hydrate phase boundary during the cooling at constant *P*.

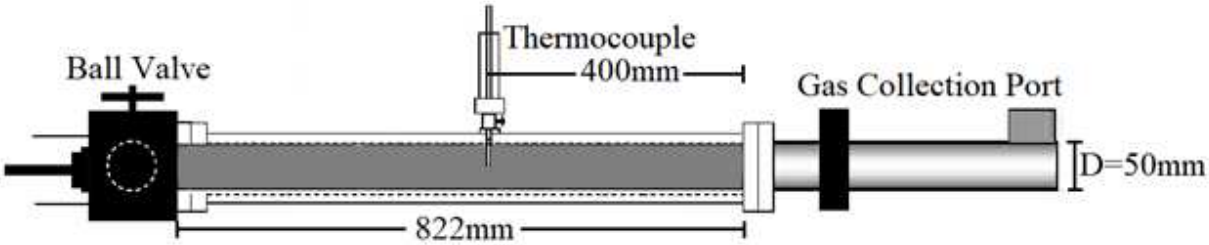

Figure 10. Schematic view of a GHBS specimen (10B-17P), indicating the position of ball-valve, and the thermocouple (Yun et al., 2011).

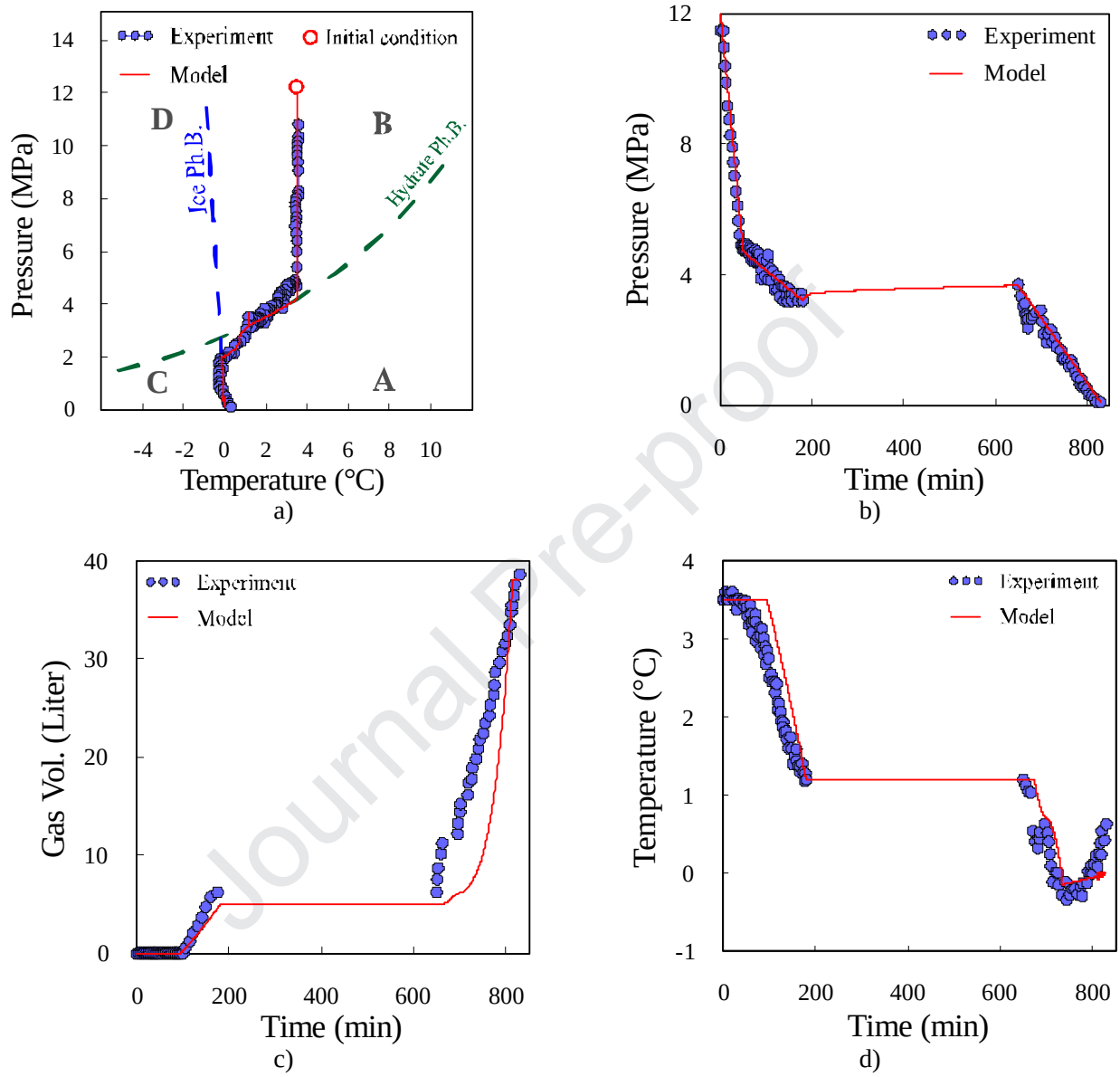

Figure 11. Depressurization-triggered gas production test results (symbols) from a natural GHBS core acquired offshore Korean (Yun et al., 2011) together with the numerical model outputs (line): a) the *P-T* path moves down at (almost) constant temperature during the depressurization in the hydrate stability zone and then diverges left on reaching the phase boundary during hydrate dissociation (because hydrate dissociation is endothermic), b) pressure reduction during the test, c) gas production during the venting experiment, and d) temperature time evolution. A slight pressure rebound was observed while the valve was closed between minutes 180 and 650 (Yun et al., 2011), feature that is properly capture by the numerical model.

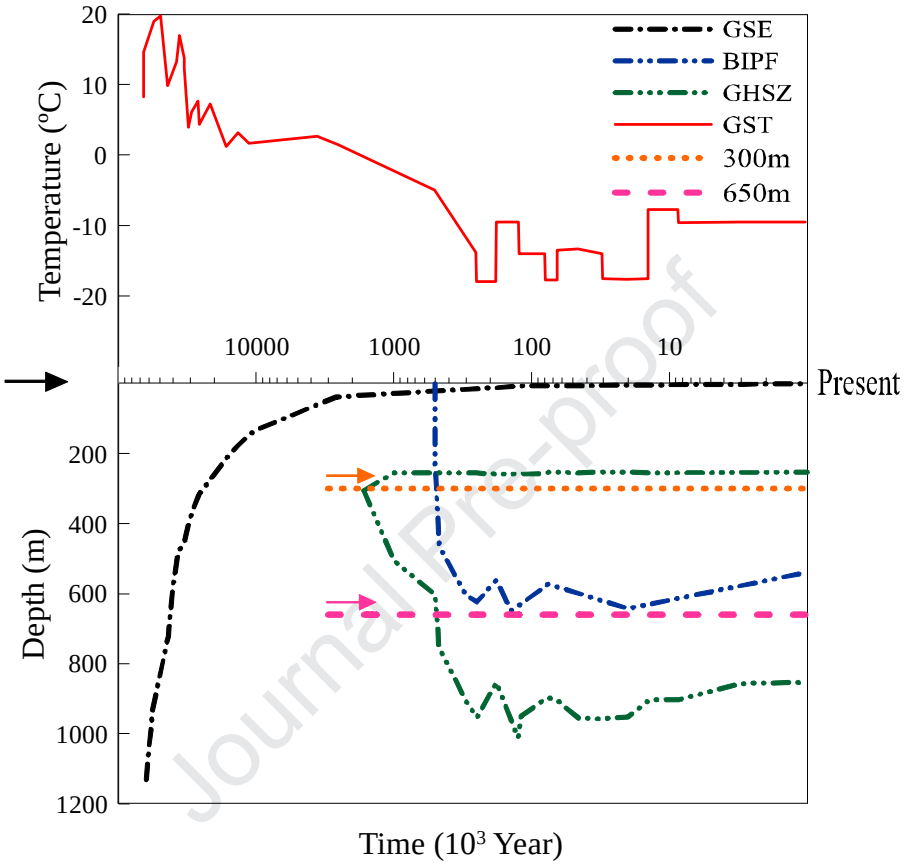

Figure 12. Time evolution of ground surface elevation (GSE), ground surface temperature (GST), base of ice bearing permafrost (BIPF), and the gas hydrate stability zone (GHSZ) at Mount Elbert site, Alaska North Slope region based on historical data (Dai et al. 2011). The depth is based on the current ground surface. The orange dotted and pink dashed lines indicate the conditions at the two target depths (i.e., 300m and 650m, respectively) for the two models (this study) with respect to the GHSZ and BIPF.

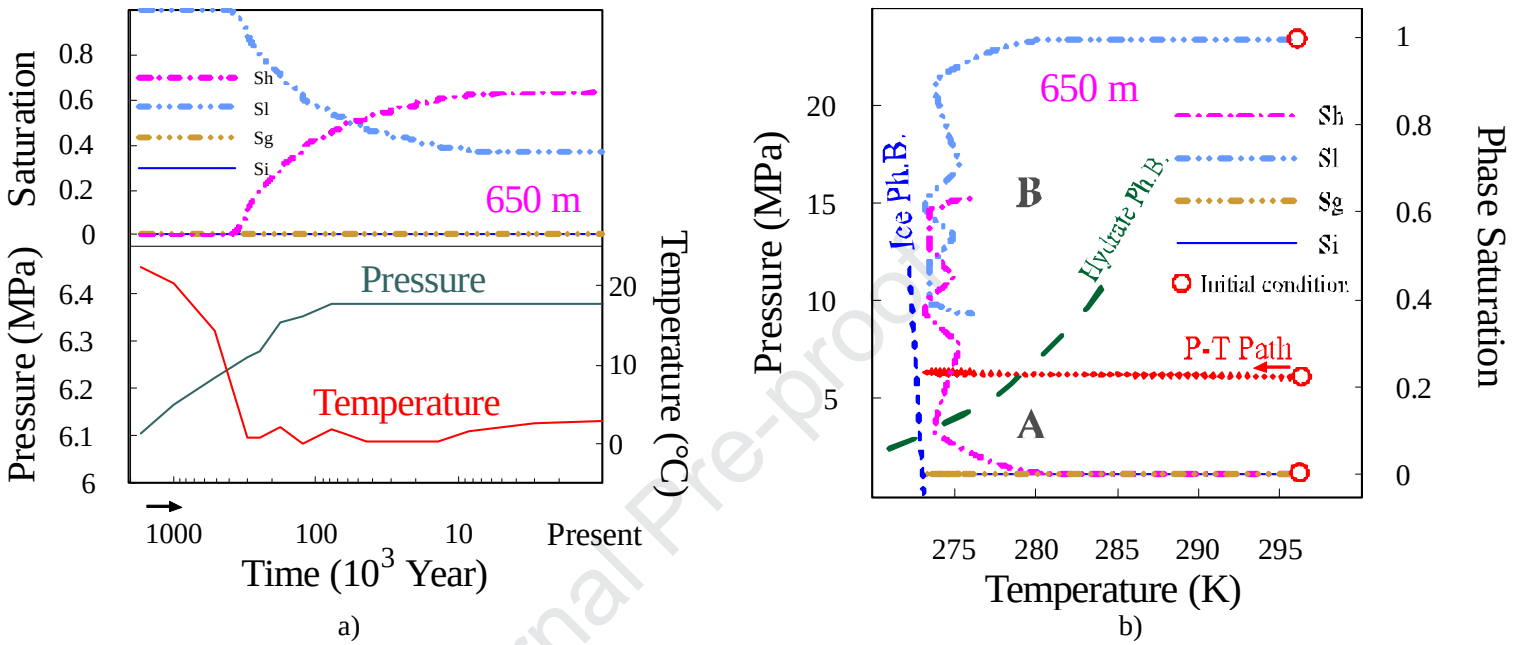

Figure 13. a) Bottom: time evolution of pressure and temperature at 650m depth (Unit C) at the Mount Elbert site, Alaska North Slope region, from Dai et al. (2011) and modeling results based on hydrostatic pore pressure from the water table at ground surface elevation and linear geothermal gradients, respectively. Top: model time evolution (current time t=0) of phase saturations associated with P and T evolutions at the corresponding depth, showing continuous hydrate formation upon continuous gas migration from under burden layers; and b) predicted evolution of phase saturations associated with the adopted P-T trajectory at 650m depth (Unit C) showing hydrate formation (i.e., from Zones A to B).

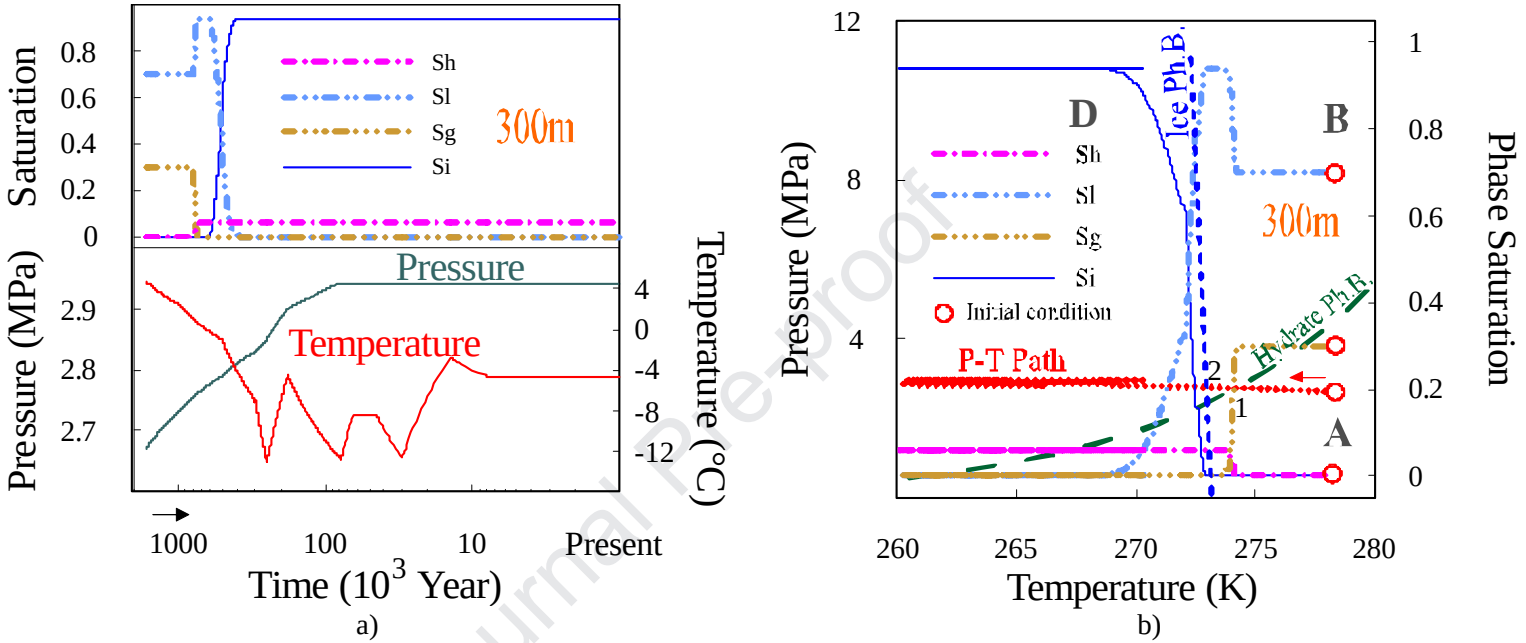

Figure 14. a) Bottom: time evolution of pressure and temperature at 300m depth at the Mount Elbert Site, Alaska North Slope region, from Dai et al. (2011) and modeling results based on hydrostatic pore pressure from the water table at ground surface elevation and linear geothermal gradients, respectively. Top: model time evolution (current time t=0) of phase saturations associated with P and T evolutions at the corresponding depth, hydrate formation is limited by the available methane gas (methane migration from lower layers is limited by low permeability strata); ice forms when temperature reduces below -1°C (i.e., the temperature at the ice bearing permafrost); b) predicted evolution of phase saturations associated with the adopted P-T trajectory at 300m depth showing limited hydrate formation (i.e., from Zones A to B), and ice formation (i.e., from Zones B to D).

1. A pseudo-kinetic model to simulate phase changes in gas hydrate bearing sediments is proposed.
2. The model is formulated in pressure-temperature (*P*-*T*) space and consists of one parameter determined from gas hydrate dissociation tests.
3. The model is validated using published dissociation tests on synthetic and natural gas hydrate.
4. The model is shown to successfully simulate cases involving different *P*-*T* paths and conditions.
5. The model is able to deal with a wide range of time scales (from hours to millions of years).

Declaration of interests

☒ The authors declare that they have no known competing financial interests or personal relationships that could have appeared to influence the work reported in this paper.

☐The authors declare the following financial interests/personal relationships which may be considered as potential competing interests: